Rheology of hexagonal-close packed (hcp) iron

Yu Nishihara [1,*], Shunta Doi [1], Noriyoshi Tsujino [2,6], Daisuke Yamazaki [2], Kyoko N. Matsukage [3], Yumiko Tsubokawa [1,4], Takashi Yoshino [2], Andrew R. Thomson [5], Yuji Higo [6], and Yoshinori Tange [6]

[1] Geodynamics Research Center, Ehime University, 2-5 Bunkyo-cho, Matsuyama, Ehime 790-8577, Japan

[2] Institute of Planetary Materials, Okayama University, 827 Yamada, Misasa, Tottori 682-0193, Japan

[3] Department of Natural and Environmental Science, Teikyo University of Science, Yamanashi 409-0193, Japan

[4] Department of Earth and Planetary Sciences, Kyushu University, 744 Motooka, Nishi-ku, Fukuoka 819-0395, Japan

[5] Department of Earth Sciences, University College London, London, WC1E 6BT, United Kingdom

[6] Japan Synchrotron Radiation Research Institute, 1-1-1 Koto, Sayo-cho, Sayo-gun, Hyogo, Japan

* To whom correspondence should be addressed.

E-mail: yunishi@sci.ehime-u.ac.jp (Y.N.).

Submitted to *Journal of Geophysical Research: Solid Earth*,

December 1, 2022

Revised May 17, 2023

Key Points

- We studied rheology of hexagonal close-packed Fe based on high-pressure and high-temperature deformation experiments
- Dominant deformation mechanism was power-law dislocation creep at temperatures above ~800 K
- We estimated the viscosity of hexagonal close-packed Fe under inner core conditions as $\geq\sim10^{19}$ Pa s

Abstract

The viscosity of hexagonal close-packed (hcp) Fe is a fundamental property controlling the dynamics of the Earth's inner core. We studied the rheology of hcp-Fe using high-pressure and -temperature deformation experiments with *in situ* stress and strain measurements. Experiments were conducted using D111-type and deformation-DIA apparatuses at pressures of 16.3–22.6 GPa, temperatures of 423–923 K, and uniaxial strain rates of 1.52×10^{-6} to 8.81×10^{-5} s^{-1} in conjunction with synchrotron radiation. Experimental results showed that power-law dislocation creep with a stress exponent of $n = 4.0 \pm 0.3$, activation energy of $E^* = 240 \pm 20$ kJ/mol, and activation volume of $V^* = 1.4 \pm 0.2$ cm^3/mol is dominant deformation mechanism at $>\sim800$ K, whereas a mechanism with power-law breakdown prevails at lower temperatures. An extrapolation of the power-law dislocation creep flow law based on homologous temperature scaling suggests the viscosity of hcp-Fe under inner core conditions is $\geq\sim10^{19}$ Pa s. If this power-law dislocation creep mechanism is assumed to be the dominant mechanism in the Earth's inner core, the equatorial growth or translation mode mechanism may be the dominant geodynamical mechanism causing the observed inner core structure.

Plain Language Summary

Although many geodynamic mechanisms have been proposed regarding the origin of the observed complex structure of Earth's inner core, no clear consensus has been reached. This is partly owing to the lack of accurate knowledge of the viscosity in the inner core, which is believed to mostly comprise of hexagonal close-packed Fe (hcp-Fe). Here, we studied the viscosity of hcp-Fe using high-pressure and high-temperature deformation experiments. The results showed that the dominant deformation mechanism in hcp-Fe changes depending on the temperature, with power-law dislocation creep and low-temperature creep being most important above and below ~800 K, respectively. Based on extrapolation of these experimental results we estimate the inner core viscosity to be $\geq 10^{19}$ Pa s. This inner core viscosity suggests the equatorial growth or translation mode model as the dominant geodynamical mechanism in the Earth's inner core.

Keywords

hcp-Fe, inner core, deformation experiments, rheology, seismic anisotropy

1. Introduction

Seismic studies have revealed the existence of anisotropic and heterogeneous structures throughout the Earth's inner core (e.g., Morelli et al., 1986; Woodhouse et al., 1986; Wang et al., 2015; Brett & Deuss, 2020; Frost et al., 2021). The single most notable structure of the inner core is that compressional waves travel ~3% faster in north-south directions, compared with those in the equatorial plane (e.g., Creager, 1992). Recent studies have further clarified the details of the inner core's structure with (i)

77 anisotropy observed to be stronger in the western hemisphere, (ii) the central portion's
78 anisotropy being tilted from polar direction, and (iii) the outer most 50–150 km being
79 nearly isotropic. Although several geodynamic mechanisms have been proposed for the
80 origin of these observed inner core structures, a clear consensus is still to be reached
81 (e.g., Sumita & Bergman, 2007; Lasbleis & Deguen, 2015; Romanowicz et al., 2016).
82 The viscosity of the inner core is one of the most important parameters in
83 determining the dominant geodynamic mechanisms occurring within the inner core.
84 Lasbleis and Deguen (2015) developed regime diagrams for inner core dynamics,
85 describing dominant mechanisms as a function of control parameters. According to their
86 analysis, in the case of unstable stratification, translation mode (global translation of the
87 inner core with solidification on one hemisphere and melting on the other) (Monnereau
88 et al., 2010) and plume convection (Jeanloz & Wenk, 1988) are predicted to be the
89 dominant mechanisms when the inner core viscosity is above and below ~10^{18} Pa s,
90 respectively. In the case of stable stratification, equatorial inner core growth
91 (deformation of inner core due to preferential growth in equatorial belt) (Yoshida et al.,
92 1996) and tangential Lorenz force (Buffett & Wenk, 2001) are regarded as the dominant
93 mechanisms when the inner core viscosity is above and below ~10^{12} Pa s, respectively.
94 An accurate understanding of the inner core viscosity is needed for a more accurate
95 constraint of the inner core dynamics.
96 The Earth's core is primarily composed of Fe with lesser amounts of Ni and light
97 elements (possible candidates are Si, S, H, O, and C) (e.g., Birch, 1952; Alfè et al.,
98 2002; Sata et al., 2010; Badro et al., 2014; Hirose et al., 2021). Although the crystal
99 structure of Fe at conditions of the inner core is considered to be hexagonal
100 close-packed (hcp) structure (e.g., Tateno et al., 2010), the viscosity of the inner core
101 has been estimated mostly based on the experimentally determined diffusion coefficient

of face-centered cubic (fcc) Fe owing to the technical difficulties of performing diffusion experiments at pressure and temperature in the hcp-Fe stability condition. The estimated viscosity values at the inner core conditions differ between published studies with estimates of $10^{20–22}$ Pa s (Reaman et al., 2012), or $\sim10^{22–25}$ Pa s (Tsujino et al., 2020) for dislocation creep. Ritterbex and Tsuchiya (2020) estimated the inner core viscosity as $\sim10^{17\pm1}$ Pa s in the dislocation creep regime based on the self-diffusion coefficient of hcp-Fe, which they calculated using density functional theory. The variation in the estimated viscosity values is partly owing to the differences in the assumed parameters (e.g., stress exponent) used to calculate viscosity using the diffusion coefficient. An experimental study in which the viscosity of hcp-Fe is directly determined from analyses of deformation experiments would provide valuable insight into the viscosity of the inner core.

Although there are number of deformation studies on hcp-Fe, most of them are focused on texture development and operating slip systems (Wenk et al., 2000; Merkel et al., 2004, 2012; Miyagi et al., 2008; Nishihara et al., 2018). On the other hand, only a limited number of experimental studies on the rheology (viscosity) of hcp-Fe have been reported. Nishiyama et al. (2007) conducted deformation experiments on hcp-Fe using a deformation-DIA apparatus (D-DIA) at a pressure (P) of 16–18 GPa and a temperature (T) of 300–600 K, and reported a stress–strain rate relationship fitted to their observations. Gleason and Mao (2013) measured deviatoric stress observed in uniaxially compressed hcp-Fe in a diamond-anvil cell up to P = 200 GPa at room temperature. Because the experimental conditions were limited to relatively low temperatures, the deformation mechanism in these studies likely differs from that occurring in the inner core, where the temperature is close to the melting temperature. This leads to a large uncertainty in the understanding of the viscosity of hcp-Fe in the

127 inner core. Deformation experiments on hcp-Fe at higher temperatures are needed.

128 In this study, the rheology of hcp-Fe was investigated by high-pressure and
129 high-temperature deformation experiments. Uniaxial deformation experiments were
130 conducted on hcp-Fe samples using D111-type and D-DIA apparatuses at P = 16.3–22.6
131 GPa, T = 423–923 K, and a uniaxial strain rate of 1.52×10^{-6} to 8.81×10^{-5} s^{-1} with the
132 stress–strain rate relationships monitored throughout *in situ* during deformation. Based
133 on these results we constrain a flow law of hcp-Fe and use it to constrain and discuss the
134 viscosity in Earth's inner core.

135

136 **2. Experimental procedures**

137 2.1. Sample preparation

138 Presintered polycrystalline iron aggregates were used in deformation experiments,
139 which were sintered by hot-pressing reagent grade Fe sponge (99.9% purity, Wako Pure
140 Chemical Industries) at ~1 GPa and 873 K in a Kawai-type multi-anvil press installed at
141 the Geodynamics Research Center, Ehime University. The sintering conditions were
142 within stability field of the body-centered cubic (bcc) structure of metallic iron, which
143 can be recovered to ambient conditions. The materials used in the experiment were
144 similar to those used in a previous study (Nishihara et al., 2018) and are known to
145 contain small amounts (<1%) of iron oxide, most likely wüstite (FeO), which had
146 formed on the surface of the grains in the starting material (see Fig. 1a of Nishihara et
147 al., 2018). The original grain size of bcc-Fe was estimated to be a few micro-meters
148 based on the distribution of the iron oxide particles. The sintered polycrystalline iron
149 samples were shaped into cylinders with a diameter of ~0.55 mm and a length of 0.5
150 mm for use in subsequent deformation experiments.

151

152 2.2. Deformation experiments

153 We performed most of the high-*P* deformation experiments with a D111-type
154 apparatus, which is a larger version of the deformation T-Cup (Hunt et al., 2014). Some
155 additional experiments (M2190, 2606, and 2609) utilized a D-DIA apparatus.
156 Experimental setups for each system are described below.

157 D111 experiments were performed at synchrotron beamline NE7A at PF-AR, KEK,
158 Tsukuba, Japan (Nishihara et al., 2020a; Tsujino et al., 2022; Thomson et al., 2023).
159 Throughout D111 experiments, 7M/2 assemblies were employed, denoting the
160 (Mg,Co)O octahedral pressure medium with 7 mm edge lengths and anvils with 2 mm
161 truncation edge lengths. In each experiment, pressure was generated using six tungsten
162 carbide anvils combined with two anvils made from either cubic boron nitride (cBN) or
163 diamond (with a SiC binder). These latter anvils are essential to allow collection of
164 azimuthal diffraction rings of the sample, which are used to determine lattice strain, and
165 subsequently stress, throughout deformation. The cell assembly (Fig. 1a) used
166 throughout experiments consists of a cylindrical graphite heater with $LaCrO_3$ thermal
167 insulator. Samples were packed in hexagonal boron nitride (hBN) sleeves and
168 sandwiched between dense Al_2O_3 pistons. In some runs, a 10 μm thick Au foil was
169 placed at either ends of sample to increase the clarity of the sample ends in X-ray
170 radiography. Temperatures were monitored using a W3%Re-W25%Re thermocouples
171 placed adjacent to the sample. The (Mg,Co)O octahedron and the $LaCrO_3$ sleeve along
172 the X-ray beam path were replaced with amorphous boron epoxy (in a ratio by weight
173 of 20:1) and hBN, respectively, to minimize X-ray absorption and diffraction from these
174 materials. Figure S1 shows the load–pressure relationship in the experiments with a
175 D111-type apparatus using the 7M/2 assembly, with pressures up to 23 GPa achieved at
176 press loads of 300 tf.

177 D-DIA experiments were performed using SPEED-MkII-D (Kawazoe et al., 2011)
178 installed on the beamline BL04B1 at the SPring-8 synchrotron facility in Japan. In these
179 runs, a cell assembly consisting of a (Mg,Co)O cubic pressure medium with 4 mm edge
180 lengths and anvils with 2.5 mm truncation edge lengths were used (Fig. 1b). Full details
181 are provided in Nishihara et al. (2018).

182 All deformation experiments, both D111-type and D-DIA apparatuses were
183 conducted in a similar manner. First, the cell assemblies were quasi-hydrostatically
184 pressurized to the desired press load before heating to the target temperature. Before
185 commencing uniaxial deformation, Fe samples were annealed at 723–923 K to ensure
186 full stabilization of hcp-structure and the sample microstructure. Annealing times varied
187 depending on the annealing temperature, such that durations were 90 min at 723 K, > 40
188 min at 823–873 K, and 25 min at 923 K. Subsequently assemblies were uniaxially
189 deformed by advancing the top and bottom anvils toward each other at a constant (and
190 controlled) D-ram displacement rate. Temperatures were controlled to within ±10 K of
191 the nominal value during deformation, with one exception (M2190-2). A total of 12
192 experiments were conducted (Table 1). Each experiment consisted of several
193 deformation steps at multiple conditions those within the range of 16.25–22.57 GPa,
194 423–923 K, and uniaxial strain rate ($\dot{\varepsilon} = d\varepsilon/dt$) of 1.52×10^{-6} to 8.81×10^{-5} s^{-1}. In
195 *stepped strain rate tests*, we changed strain rate stepwise during one run at nearly
196 constant *P* and *T* conditions. Similarly, in the *stepped temperature* and *pressure tests*,
197 only the temperature or pressure were altered in a stepwise manner. After the
198 completion of each series of deformation conditions, the power was shut off to
199 temperature quench the experiment. Because the temperature reported in this paper is
200 the nominal temperature measured at a slightly off-center part of the assembly, the
201 average temperature of the specimens may have been higher by up to 10–50 K, since

202 temperature gradients in high-pressure cell assemblies can be significant over
203 sub-millimetre distances (Raterron et al., 2013). We ignored the effect of pressure on the
204 temperature measurements using a W3%Re-W25%Re thermocouple because the
205 estimated pressure effect is comparable to, or smaller than, the above temperature
206 uncertainty (Nishihara et al., 2020b).
207
208 2.3. Stress and strain measurements
209 During the deformation experiments, synchrotron radiation was employed to
210 observe *in situ* changes in the sample's strain and stress through a combination of
211 imaging and diffraction data collections. To achieve this, the incident X-rays were first
212 monochromatized to around 60 keV using a Si (111) monochromator. A motorized stage
213 with gadolinium aluminum gallium garnet (GAGG) or yttrium aluminum garnet (YAG)
214 scintillators coupled to a CMOS or CCD camera was used to capture X-ray radiographic
215 images, with exposure times ranging from 1 to 30 seconds. Sample strain was calculated
216 by analyzing the absorption contrast between the sample and Al_2O_3 pistons (or the
217 position of Au foil markers in some runs) in the X-ray radiographs (Fig. 2a) using NIH
218 Image-J software. The uniaxial strain was then determined using the formula $\varepsilon =$
219 $-\ln(l/l_0)$, where l and l_0 represent the sample length during and before deformation,
220 respectively. An example of the strain changes during the Iron25 run is shown in Figure
221 2b. Furthermore, the strain rate ($\dot{\varepsilon}$) during each experiment (and at each deformation
222 step) was determined by fitting a linear equation to the series of strain–time data.
223 To calculate sample stress, two-dimensional angle-dispersive X-ray diffraction was
224 used. The monochromatic X-rays were collimated using horizontal and vertical slits
225 mounted on a motorized stage, with a size of 200 × 200 μm or smaller depending on the
226 sample shape and anvil gap width. Diffraction images were collected using a CMOS

227 flat-panel detector (Dexela 2923, sensitive area of 291 mm × 230 mm, pixel size of
228 0.075 mm) or a CCD detector (MarCCD, sensitive area of 200 mm diameter circle,
229 pixel size of 0.050 mm) at a distance of 541–641 mm from the sample with an exposure
230 time of 60–600 s. To calibrate incident X-ray energy and sample-detector geometry, a
231 CeO_2 standard was placed at the sample position prior to high-pressure runs. Examples
232 of the two-dimensional X-ray diffraction images in the experiments using D111-type
233 and D-DIA apparatuses are shown in Figure 3a and 3b, respectively.

234 Four distinct diffraction peaks of hcp-Fe ($10\bar{1}0$, 0002, $10\bar{1}1$, and $10\bar{1}2$) were used to
235 analyze stress and pressure. Each diffraction image was subdivided into 36 azimuthal
236 sectors with equal azimuth angles η of 10º, and integrated separately using a software
237 IPAnalyzer (Seto et al., 2010). Position of the sample diffraction peaks in each
238 azimuthal bin were determined by fitting a symmetric pseudo-Voigt function to each
239 integrated one-dimensional diffraction pattern using PDIndexer (Seto et al., 2010). This
240 allows determination of the *d* spacings from sample diffraction peaks as a function of
241 diffraction azimuth. Stress in the uniaxial deformation experiments was subsequently
242 determined by fitting the following equation (e.g., Nye, 1985; Singh, 1993; Uchida et al.,
243 1996; Singh et al., 1998);

244 $$d_{hkl}(\psi) = d^0_{hkl}\left\{1 + (1 - 3\cos^2\psi)\frac{\sigma}{6\langle G_{hkl}\rangle}\right\} \quad (1)$$

245 where ψ is the angle between the direction normal to the diffracting plane and the
246 maximum principal stress direction, $d_{hkl}(\psi)$ is the observed *d* spacing as a function of
247 the ψ angle, d^0_{hkl} is the *d* spacing corresponding to the hydrostatic pressure; σ is the
248 uniaxial stress calculated for a given diffraction peak with the Miller index *hkl*, and
249 $\langle G_{hkl}\rangle$ is the effective shear modulus for a given *hkl* at the corresponding *P–T* condition.
250 The relationship between the angles η and ψ is expressed by $\cos\psi = \cos\theta\cdot\cos(\eta - \eta_{max})$
251 where θ is the diffraction angle, and η_{max} is the η angle at which $d_{hkl}(\psi)$ is the

252 minimum (corresponding to the maximum principal stress direction) (see Merkel et al.,
253 2002). Figure 3c shows examples of $d_{hkl}(\psi)$–ψ data and the fits of Equation (1). The
254 $\langle G_{hkl} \rangle$ term was calculated from the elastic constants (C_{ij}) of hcp-Fe at corresponding P–
255 T conditions using equations described by Singh et al. (1998). We assume a uniform
256 stress condition in the calculation of $\langle G_{hkl} \rangle$ (α =1 in Equation (4) of Singh et al., 1998)
257 and calculated the C_{ij} terms at high-P and high-T conditions based on Sha and Cohen
258 (2010a, 2010b). The pressure was calculated by using the unit cell volume of iron,
259 which was obtained from the d^0_{hkl} values, extracted from the fitted azimuthal patterns
260 (Equation (1)), and the thermal equation of state of hcp-Fe as reported in Uchida et al.
261 (2001) and Sakamaki et al. (2009).
262
263 **3. Results**
264 3.1. Experimental conditions
265 Table 1 summarizes the conditions and results of the deformation experiments.
266 Figure 4 compares the P–T conditions of the deformation experiments with the stability
267 field of hcp-Fe. We primarily conducted the deformation experiments in the
268 high-temperature region of the stability field of hcp-Fe in the studied pressure range.
269 The obtained data mostly fell within at P ~ 17 GPa with a few points at higher pressures
270 up to 23 GPa. The bcc-Fe starting material was partially or completely transformed to
271 hcp-Fe after compression at 300 K in all experiments, except for run M2609. The
272 sample completely transformed, within the detection limits of the diffraction images,
273 into an hcp structure during annealing at >723 K in all runs.
274
275 3.2. Texture development
276 Development of texture was observed in the D-DIA experiments. Figure 3b shows

two-dimensional X-ray diffraction image taken at the final stage of deformation in M2609. The Debye ring of 0002 diffraction is more intense at top and bottom whereas that of $10\bar{1}0$ diffraction is at right and left suggesting basal plane normal is preferentially oriented subparallel to the compression axis. Similar observation was reported by Nishihara et al. (2018). Development of texture suggests dislocation glide played important role in these experiments. In the experiments using D111-type apparatus, observation of texture developed throughout deformation is more challenging. This is because of the larger anvils required in D111 experiments, the intensity difference between X-ray only transiting the anvil gap and those passing through cBN or sintered diamond anvils is far larger, which obscures intensity variations originating from sample texture.

3.3. Mechanical results

Figure 5 shows the variations in stress and pressure during selected deformation experiments. The pressure was approximately constant in all deformation steps. Steady state was generally achieved after deformation with a strain (ε) of 0.02 in each step. In the steady-state deformation, applied stress and microstructure are regarded to be dynamically balanced with combination of concurrent processes such as dislocation glide, dynamic recrystallization and recovery maintaining equilibrium. The steady-state stress value in each run increased with increasing strain rate and pressure and decreasing temperature. The stress values calculated from four diffraction peaks differed, especially at higher-stress conditions, where the stress value by $10\bar{1}0$ was always the highest and that by $10\bar{1}2$ was generally the lowest among the four peaks. This tendency is consistent with that reported in previous studies (Nishiyama et al., 2007; Merkel et al., 2012; Nishihara et al., 2018). The difference of stress values between diffraction peaks

primarily corresponds to difference in magnitude of the lattice distortion, and is also partly influenced by difference in $\langle G_{hkl} \rangle$ value (elastic anisotropy). This is due to the heterogeneous stress–strain distribution in the polycrystalline specimen caused by plastic anisotropy (orientation dependence of viscosity) (e.g., Castelnau et al., 2008). In M2190-2, during deformation at 723 K, the temperature instantaneously dropped ~400 K for a few seconds and then recovered to 723 K, possibly due to deformation or buckling of the graphite heater. We used the data obtained in M2190-2 for the following analysis because no remarkable change occurred in the strain or stress behavior before and after the drop and recovery in temperature. For Iron17-1, we performed deformation at 923 K, the highest temperature achieved in this study, but at these conditions the steady state-stress was observed to below the detection limits.

Figure 6a shows a log-log plot of the strain rate versus stress in the stepped strain rate tests (note that the error bars in Figures 6a, 6b, and 7a–d represent the range of stresses determined by four diffraction peaks, not stress uncertainties). In these tests, we determined steady-state stress at different strain rates under a constant temperature and nearly constant pressure. Differential sample stress is observed to be temperature dependent; stress was ~2 GPa at 523 K and decreased with increasing temperature to 0.3–0.5 GPa at 873 K. The data from each run mostly showed power-law behavior (i.e., $\dot{\varepsilon} \propto \sigma^n$). The slope of varying stress exponent (n) is indicated in the lower right of Figure 6a. Stress exponents of ~3–5 were observed at temperatures higher than ~800 K and, whereas n appears to be >5 at lower temperatures. The stress values previously reported by Nishiyama et al. (2007) at lower temperatures (400 and 600 K) and P = 15.9–17.5 GPa are consistent with our data at similar temperatures and strain rate (crosses in Fig. 6a). The stress exponent obtained at 600 K by Nishiyama et al. (2007) ($n \sim 6$) was lower than that obtained in this study ($n > 10$). This could have been related

327 to the extremely strong preferred orientation in Nishiyama et al.'s (2007) experiments
328 where bcc-Fe rod was employed as a starting material.

329 Figure 6b shows the Arrhenius plot of stress versus reciprocal temperature for the
330 stepped temperature tests. Each of these tests was conducted at nearly constant strain
331 rate and pressure. The slope of this plot is proportional to H^*/n, where H^* is the
332 activation enthalpy. Above ~800 K, the H^*/n value was ~60 kJ/mol, judging from the
333 steep slope in the plot. At lower temperatures, the H^*/n value drastically decreased with
334 decreasing temperature. The changes in temperature dependence and n value (Fig. 6a)
335 consistently suggested a transition in the deformation mechanism at ~800 K.

336 Figure 6c is a semilog plot of stress versus pressure for the stepped pressure test
337 (Iron14) at a constant temperature of 823 K and nearly constant strain rate of 1.1–1.3 ×
338 10^{-5} s^{-1}. The steady-state stress values at P = 21.4 GPa were slightly higher than those
339 at P = 16.6 GPa. Although the pressure dependence of the stress slightly differed
340 depending on the diffraction peaks, the slopes indicated in this plot are generally gentle
341 suggesting that the V^*/n value was substantially lower than 1 cm^3/mol (V^* is the
342 activation volume).

343 The mechanical data for each run were not fully consistent owing to the run-to-run
344 variability. The most notable example is shown in Figure 6a: the stress values of runs
345 Iron01 and Iron12 differed by a factor of ~2 at a strain rate of ~4 × 10^{-6} s^{-1}, although we
346 conducted both these runs at the same temperature (823 K) and pressure (16.4−17.4
347 GPa). One possible reason for this run-to-run variability is the run-to-run difference in
348 the position of the thermocouple junction. Even though the design of the cell assembly
349 (Fig.1) was practically identical throughout this study, a small change in the position of
350 the thermocouple junction could have occurred. This could have led to a systematic
351 difference in the temperature from run to run. Another explanation for the run-to-run

variability is the run-to-run difference in hydrogen content (e.g., Hayashi et al., 1998). Although we conducted the experiments under nominally anhydrous conditions, a small amount of water may have adsorbed to the pressure medium from the moisture in the air and hydrogen may have been incorporated in sample. Because rheology can be highly sensitive to differences in the chemical and physical environments, run-to-run variability is unavoidable. However, the data derived in a single run would be consistent because the chemical and physical environments remain essentially unchanged in a single run. Therefore, run-to-run variability must be corrected to accurately determine flow law parameters and deformation mechanisms.

4. Discussion

4.1. Interpretation of rheological behavior

As described above, the mechanical data of hcp-Fe suggests the occurrence of differing mechanisms at temperatures above and below ~800 K (Figs. 6a, 6b). Based on this observation, we analyzed the mechanical data at >800 K and <800 K separately.

At >800 K, the observed stress exponent was $n \sim 3-5$ (Fig. 6a), which is in the range of common values for the power-law dislocation creep of metals (e.g., Mukherjee, 2002). The constitutive equation for power-law dislocation creep is:

$$\dot{\varepsilon} = A_{\mathrm{PL}} \sigma^{n_{\mathrm{PL}}} \exp\left(-\frac{E^*_{\mathrm{PL}} + PV^*_{\mathrm{PL}}}{RT}\right) \qquad (2)$$

where $\dot{\varepsilon}$ is the strain rate, A is the pre-exponential constant, σ is the deviatoric stress, E^* is the activation energy, V^* is the activation volume, and R is the gas constant. The subscript PL represents parameters for power-law dislocation creep. For successful data analysis via Equation (2), the observed run-to-run variability needed to be corrected.

This was achieved using a similar approach to that used by Keefner et al. (2011), developed to analyze deformation experiments on olivine aggregates in a dislocation creep regime at P = 300 MPa. In this study the authors precisely determined the flow-law parameters using a global fit of the constitutive equation to derived mechanical data with a correction for run-to-run variability by multiplying the pre-exponential constant, A, by parameter, α, where α differs between runs. We adopted similar correction approach in this study, but instead of correcting pre-exponential factor, A, we applied a run-to-run correction on the observed stress, σ_{obs}. The correction parameter, β, was used such that the corrected stress (σ_{cor}) is determined as $\sigma_{cor} = \beta \times \sigma_{obs}$. Therefore, Equation (2) becomes:

$$\dot{\varepsilon} = A_{\mathrm{PL}}(\beta\sigma_{\mathrm{obs}})^{n_{\mathrm{PL}}}\exp\left(-\frac{E^*_{\mathrm{PL}}+PV^*_{\mathrm{PL}}}{RT}\right). \qquad (3)$$

Where β differs for each run, but is close to one when the run-to-run variability is small. The correction was applied to stress rather than pre-exponential constant in this study because, in the case of $n > 1$, as in this study, the required correction magnitude becomes smaller when a correction is applied to stress.

Equation (3) was fitted to the data at high temperatures (>800 K) whereby the values of β for all runs were simultaneously adjusted to minimize $\sum_i(\log\beta_i)^2$ (β_i is β for a run i) providing the best fitting β values close to one. Fitting results are shown in Figures 7a and 7b. The derived flow-law parameters and β values are presented in Tables 2 and S1, respectively. The stress correction parameter β ranged between 0.678 and 1.332. These corrections are equivalent to temperature deviations of +39 to −27 K (at 873 K and 17 GPa) assuming that the entirety of the run-to-run variability is attributable to the temperature errors. The determined flow-law parameters are n = 4.0 ±

0.3, E^* = 240 ± 20 kJ/mol, and V^* = 1.4 ± 0.2 cm^3/mol. Activation enthalpy, H^* (= E^* + PV^*), at P = 17 GPa was calculated to be 260 ± 20 kJ/mol. These values suggest that the dominant deformation mechanism of hcp-Fe at >800 K is dislocation creep, the rate-limiting process of which is dislocation climb (Weertman creep). The stress exponent (n = 4.0) falls within the range of typical Weertman creep values of hcp metals, $3.0 \leq n \leq 5.5$ (Mukherjee, 2002).

In Weertman creep, the activation enthalpy, and hence the activation energy and volume, are comparable to that of lattice diffusion (e.g., Frost & Ashby, 1982). Although no experimental study has been published on the diffusion coefficient for the lattice diffusion of hcp-Fe, Ritterbex and Tsuchiya (2020) calculated the self-diffusion coefficient of hcp-Fe based on density functional theory. Their results included an H^* at P = 17 GPa and V^* of 500 kJ/mol and 3.0 cm^3/mol, respectively, for hcp-Fe. These values are considerably higher than those obtained for power-law creep at >800 K in this study. On the other hand, the H^* of hcp-Fe at 17 GPa was estimated to be 290 kJ/mol based on a universal relationship between the melting temperature and diffusion coefficient for hcp metals (Brown & Ashby, 1980) using the fictive melting temperature of hcp-Fe at 17 GPa as 1990 K (Anderson & Isaak, 2000), which is fairly consistent with the results of this study.

The diffusion coefficient for the lattice diffusion of hcp-Fe is generally assumed to be close to that of fcc-Fe because both hcp and fcc are close-packed structures. E^* for self-diffusion in fcc-Fe is approximately 270 kJ/mol (Frost & Ashby, 1982). Based on high-pressure experiments by Yunker and Van Orman (2007), H^* and V^*at P = 17 GPa for Fe-Ni inter-diffusion in a fcc-structured Fe–Ni alloy were determined to be 365 kJ/mol and 3.1 cm^3/mol, respectively. Compared with the activation parameters of diffusion for fcc-Fe, the E^*, H^*, and V^* values of the power-law dislocation creep of

hcp-Fe in this study are consistent (E*) or somewhat lower. Therefore, although we are not fully certain that the power-law creep at >800 K in this study was rate-limited by dislocation climb and hence lattice diffusion, it is our preferred interpretation that the observed deformation mechanism was Weertman creep, which may be dominant at higher temperatures near the melting temperature.

At temperatures lower than 800 K, the stress exponents were larger (Fig. 6a), and the temperature dependence of the deviatoric stress was smaller (Fig. 6b). The most common low-temperature deformation mechanism in metals is a type of power-law creep (e.g., Frost & Ashby, 1982) whereby diffusion along the dislocation line (pipe diffusion) is the rate-limiting process. At low temperatures, a power-law breakdown is commonly observed, where the stress exponent is no longer constant (e.g., Frost & Ashby, 1982). The power-law breakdown is commonly recognized as transition of mechanism from dislocation climb-controlled flow to dislocation glide-controlled flow. The constitutive equation for low-temperature power-law creep with a power-law breakdown is:

$$\dot{\varepsilon} = A_{\mathrm{LT}}\sigma_{\mathrm{cor}}{}^{n_{\mathrm{LT}}}\exp\left(-\frac{E^*_{\mathrm{LT}}+PV^*_{\mathrm{LT}}}{RT}\left\{1-\left(\frac{\sigma_{\mathrm{cor}}}{\sigma_{\mathrm{P}}}\right)^p\right\}^q\right) \quad , \qquad (4)$$

where σ_{P} is the Peierls stress; p and q are constants that are generally bounded as $0 \leq p \leq 1$ and $1 \leq q \leq 2$, respectively. The subscript LT represents parameters for the low-T mechanism. Equation (4) was fitted to the experimental data from this study at conditions of <800 K. Again the observed run-to-run variability was corrected using the stress correction parameter, β, as described above. β was fixed = 1 for runs M2606, 2609, and 2190, in which the temperature was <800 K throughout the experiments. We

assumed $n = 5$, which is a common value for the low-temperature power-law creep of metals. The E^* and V^* for the low-temperature mechanism, and hence pipe diffusion, were assumed to be close to those for grain-boundary diffusion (Frost & Ashby, 1982). We estimated the E^* and V^* for the low-temperature mechanism of hcp-Fe by multiplying the E^* and V^* for the high-temperature mechanism by 10.8/17.3 following the empirical relationship between Arrhenius parameters for grain-boundary diffusion and lattice diffusion presented by Brown and Ashby (1980) (Table 2). Values of A, σ_P, p, and q were manually adjusted to best fit the data, as automatic fitting algorithms were found to be unstable (Table 2). Although q is generally within the range of $1 \leq q \leq 2$, a small value ($q = 0.1$) was required to fit our experimental data. This drastically changes the temperature dependence of stress (Fig. 6b).

Figures 7c and 7d show the fits of the flow-law equations of the high- and low-temperature mechanisms (power-law and low-T creeps, respectively) at a normalized pressure of 17 GPa. Assuming that the mechanisms at high and low temperatures were independent, the total strain rate could be expressed as the sum of the strain rates of the two mechanisms (Equations (3) and (4)). As shown in these figures, the flow-law equations provide good fits to the experimental observations from this study, suggesting the above analysis was appropriate.

4.2. Implications for inner core viscosity

Based on the above findings, the high-temperature deformation mechanism (power-law dislocation creep), assuming there are no pressure-induced changes in deformation mechanism, may be the dominant mechanism in the Earth's inner core. Making this assumption the above determined flow law was extrapolated to conditions of the inner core based on homologous temperature scaling (Fig. 8). In the homologous

476 temperature scaling, the activation enthalpy is expressed through melting temperature
477 (T_m) as $H^* = gRT_m$, where g is semi-empirical constant (e.g., Brown & Ashby, 1980).
478 By susbstituting gRT_m for $E^* + PV^*$ (= H^*) in Equation (2), the following equation can
479 be used in the extrapolation:
480
481 $$\dot{\varepsilon} = A_{\mathrm{PL}} \sigma^{n_{\mathrm{PL}}} \exp\left(-g \frac{T_m}{T}\right) \quad . \quad (5)$$
482
483 The g value for hcp-Fe was determined to be 15.8 using values of H^* and T_m at P = 17
484 GPa (260 kJ/mol and 1990 K (Anderson & Isaak, 2000), respectively). Extrapolation of
485 this relationship was undertaken to a commonly accepted inner core temperature of
486 T_m/T = 1.1 and a stress of 10^2 Pa (= 10^{-7} GPa) because the inner core stress has
487 generally been regarded as $\leq 10^4$ Pa (e.g., Yoshida et al., 1996; Buffett, 1997; Karato,
488 1999).
489 To evaluate the possible contribution of diffusion creep (Nabarro–Herring creep),
490 we calculated the stress–strain rate relationship at T_m/T = 1.1 using a rate equation (e.g.,
491 Karato, 2008) with the reported diffusion coefficient of fcc-Fe (Yunker & Van Orman,
492 2007). As shown in Figure 8, the strain rate of diffusion creep for grain size (d) of > 1 m
493 (e.g., Bergman, 1998; Yamazaki et al., 2017) is lower than that of power-law dislocation
494 creep under the most probable stress range in the inner core, 10^3–10^4 Pa (= 10^{-6}–10^{-5}
495 GPa). Therefore, diffusion creep does not appear to be a dominant deformation
496 mechanism in the Earth's inner core. This conclusion is reasonable because diffusion
497 creep hardly yields crystallographic preferred orientation, and hence, it should not able
498 to explain the observed seismic anisotropy.
499 At the stress condition of $\leq 10^4$ Pa (Yoshida et al., 1996; Buffett, 1997; Karato, 1999;
500 Van Orman, 2004), the viscosity and strain rate for power-law dislocation creep were

calculated to be $\geq 10^{19.1 \pm 2.2}$ Pa s and $\leq 10^{-15.1 \pm 2.2}$ s^{-1}, respectively. According to Lasbleis and Deguen (2015), plume convection and tangential Lorentz force mechanisms do not appear when the inner core viscosity is $>10^{18}$ Pa s. Thus, if the power-law creep (following the flow law determined in this study) is dominant in the inner core, equatorial growth and translation mode are the viable candidates as the dominant geodynamic mechanisms. The equatorial growth mechanism has been regarded as one of the most probable candidates for the dominant inner core dynamics, by which formation of seismic anisotropy with several percent level can be reasonably explained under some conditions with compositional stratification, pretexture, or inner core translation (e.g., Lincot et al., 2016; Frost et al., 2021). Our conclusion supports this model.

Although we have assumed power-law creep, as inferred from experiments in this study, as a dominant deformation mechanism in the above discussion, other deformation mechanisms are also possibly dominant in the Earth's inner core. Harper–Dorn creep is often regarded as the dominant deformation mechanism in the inner core (e.g., Van Orman, 2004, Tsujino et al., 2020), which appears under low stress and large-grain conditions, but its mechanism is not fully understood, and its existence has been the subject of debate (e.g., Kassner et al., 2007). If Harper-Dorn creep is the dominant deformation mechanism, the inner core viscosity may be lower than the above estimate, and thus the discussion on the Earth's inner core dynamics could be revised.

We also note that throughout the above discussion a rheology relevant for pure Fe, neglecting the effect of compositional variation, has been assumed representative of the inner core. However, incorporation of light element(s) (e.g., H, Si, S) can have potentially significant influence on the rheology of hcp-Fe. Further studies investigating this issue are desirable for accurate understanding of the inner core dynamics.

5. Conclusion

Rheology of hcp-Fe was determined via uniaxial deformation experiments performed using D111-type and D-DIA apparatuses at P = 16.3–22.6 GPa, T = 423–923 K. The results showed that the dominant deformation mechanism in hcp-Fe changes depending on the temperature, with power-law dislocation creep and low-temperature creep dominate above and below ~800 K, respectively. An extrapolation of the derived flow law for power-law dislocation creep based on homologous temperature scaling suggested that the viscosity of hcp-Fe under inner core conditions is $\geq\sim10^{19}$ Pa s. If the power-law dislocation creep is assumed to be the dominant mechanism in the Earth's inner core, the equatorial growth or translation mode mechanism may be the dominant geodynamical mechanism.

Acknowledgements

We thank A. Suzuki, T. Kubo, and N. Funamori for their helpful support with the *in situ* deformation experiments, and T. Ohuchi and S. Ritterbex for their constructive discussions. We also thank E. Takahashi for providing sintered diamond anvils, and K. Nishida, and R. Iizuka-Oku for developing the X-ray radiograph system at KEK. In situ deformation experiments were performed using a D111-type system at NE7A, PF-AR at KEK (proposal numbers 2016G016, 2017PF-02, 2017PF-07, and 2018G059) and the SPEED-MkII-D system at BL04B1 in SPring-8 (proposal numbers 2017A0075 and 2018B0075). This study was supported by the Japan Society for the Promotion of Science (JSPS) under Grant-in-Aid for Scientific Research (A) (19H00723) and (B) (15H03749), and Grant-in-Aid for Innovative Areas (15H05827). Constructive comments by J. Van Orman and an anonymous reviewer are appreciated.

551

552 **Data Availability Statements**

553 The datasets for this study are available at https://doi.org/10.5281/zenodo.7273263.

554

555 **References**

556 Alfè, D., Gillan, M.J., & Price, G.D. (2002). Composition and temperature of the
557 Earth's core constrained by combining ab initio calculations and seismic data. *Earth*
558 *and Planetary Science Letters*, *195*(1-2), 91-98.
559 https://doi.org/10.1016/S0012-821X(01)00568-4

560 Anderson, O.L., & Isaak, D.G. (2000). Calculated melting curves for phases of iron.
561 *American Mineralogist*, *85*(2), 376-385. https://doi.org/10.2138/am-2000-2-317

562 Badro, J., Côté, A.S., & Brodholt, J.P. (2014). A seismologically consistent
563 compositional model of Earth's core. *Proceedings of the National Academy of*
564 *Sciences*, *111*(21), 7542-7545. https://doi.org/10.1073/pnas.1316708111

565 Bergman, M.I. (1998). Estimates of the Earth's inner core grain size. *Geophysical*
566 *Research Letters*, *25*(10), 1593-1596. https://doi.org/10.1029/98GL01239

567 Birch, F. (1952). Elasticity and constitution of the Earth's interior. *Journal of*
568 *Geophysical Research*, 57(2), 227-286. https://doi.org/10.1029/JZ057i002p00227

569 Brett, H., & Deuss, A. (2020). Inner core anisotropy measured using new ultra-polar
570 PKIKP paths. *Geophysical Journal International*, *223*(2), 1230-1246.
571 https://doi.org/10.1093/gji/ggaa348

572 Brown, A.M., & Ashby, M.F. (1980). Correlations for diffusion constants. *Acta*
573 *Metallurgica*, *28*(8), 1085-1101. https://doi.org/10.1016/0001-6160(80)90092-9

574 Buffett, B.A. (1997). Geodynamic estimates of the viscosity of the Earth's inner core.
575 *Nature*, *388*, 571-573. https://doi.org/10.1038/41534

576 Buffett, B.A., & Wenk, H.-R. (2001). Texturing of the Earth's inner core by Maxwell
577 stresses. *Nature*, *413*, 60-63. https://doi.org/10.1038/35092543
578 Bundy, F.P. (1965). Pressure-temperature phase diagram of iron to 200 kbar, 900ºC.
579 *Journal of Applied Physics*, *36*(2), 616-620. https://doi.org/10.1063/1.1714038
580 Castelnau, O., Blackman, D.K., Lebensohn, R.A., & Castaneda, P.P. (2008).
581 Micromechanical modeling of the viscoplastic behavior of olivine. *Journal of*
582 *Geophysical Research: Solid Earth*, *113*(B9), B09202.
583 https://doi.org/10.1029/2007JB005444
584 Creager, K.C. (1992). Anisotropy of the inner core from differential travel times of the
585 phases PKP and PKIKP. *Nature*, *356*, 309-314. https://doi.org/10.1038/356309a0
586 Frost, H.J., & Ashby, M.F. (1982). *Deformation Mechanism Maps: The Plasticity and*
587 *Creep of metals and Ceramics*. Oxford, U.K., Pergamon Press.
588 Frost, D.A., Lasbleis, M., Chandler, B., & Romanowicz, B. (2021). Dynamic history of
589 the inner core constrained by seismic anisotropy. *Nature Geoscience*, *14*, 531-535.
590 https://doi.org/10.1038/s41561-021-00761-w
591 Gleason, A.E., & Mao, W.L. (2013). Strength of iron at core pressures and evidence for
592 a weak Earth's inner core. *Nature Geoscience*, *6*, 571-574.
593 https://doi.org/10.1038/ngeo1808
594 Hayashi, E., Kurokawa, Y., & Fukai, Y. (1998) Hydrogen-induced enhancement of
595 interdiffusion in Cu-Ni diffusion couples. *Physical Review Letters*, *80*(25),
596 5588-5590. https://doi.org/10.1103/PhysRevLett.80.5588
597 Hirose, K., Wood, B., & Vočadlo, L. (2021) Light elements in the Earth's core. *Nature*
598 *Reviews*, *2*, 645-658. https://doi.org/10.1038/s43017-021-00203-6
599 Hunt, S.A., Weidner, D.J., McCormack, R.J., Whitaker, M.L., Bailey, E., Li, L.,
600 Vaughan, M.T., & Dobson, D.P. (2014). Deformation T-Cup: a new multi-anvil

apparatus for controlled deformation experiments at pressures above 18 GPa. *Review of Scientific Instruments*, *85*(8), 085103. https://doi.org/10.1063/1.4891338

Karato, S. (1999). Seismic anisotropy of the Earth's inner core resulting from flow induced by Maxwell stresses. *Nature*, *402*, 871-873. https://doi.org/10.1038/47235

Karatro, S. (2008). *Deformation of Earth Materials: An Introduction to the Rheology of Solid Earth*. Cambridge, U.K., Cambridge Univ. Press. https://doi.org/10.1017/CBO9780511804892

Kassner, M.E., Kumar, P., & Blum, W. (2007) Harper−Dorn creep. *International Journal of Plasticity*, *23*, 980–1000. https://doi.org/10.1016/j.ijplas.2006.10.006

Kawazoe, T., Nishihara, Y., Ohuchi, T., Nishiyama, N, Higo, Y., Funakoshi, K., & Irifune, T. (2011). In situ stress-strain measurements in a deformation-DIA apparatus at P-T conditions of the upper part of the mantle transition zone. *American Mineralogist*, *96*(11-12), 1665-1672. https://doi.org/10.2138/am.2011.3818

Keefner, J.W., Mackwell, S.J., Kohlstedt, D.L., & Heidelbach, F. (2011). Dependence of dislocation creep of dunite on oxygen fugacity: Implications for viscosity variations in Earth's mantle. *Journal of Geophysical Research: Solid Earth*, *116*(B5), doi:10.1029/2010JB007748. https://doi.org/10.1029/2010JB007748

Lasbleis, M., & Deguen, R. (2015). Building a regime diagram for the Earth's inner core. *Physics of the Earth and Planetary Interiors*, *247*, 80-93. https://doi.org/10.1016/j.pepi.2015.02.001

Lincot, A., Cardin, P., Deguen, R., & Merkel, S. (2016) Multiscale model of global inner-core anisotropy induced by hcp alloy plasticity. *Geophysical Research Letters*, *43*, 1084-1091. https://doi.org/10.1002/2015GL067019

Merkel, S., Wenk, H.R., Shu, J., Shen, G., Gillet, P., Mao, H.-k., & Hemley., R.J. (2002). Deformation of polycrystalline MgO at pressures of the lower mantle. *Journal of*

626 *Geophysical Research: Solid Earth*, *107*(B11), 2271.
627 https://doi.org/10.1029/2001JB000920
628 Merkel, S., Wenk, H.-R., Gillet, P., Mao, H.-k., & Hemley, R.J. (2004) Deformation of
629 polycrystalline iron up to 30 GPa and 1000 K. *Physics of the Earth and Planetary*
630 *Interiors*, *145*, 239-251. https://doi.org/10.1016/j.pepi.2004.04.001
631 Merkel, S., Gruson, M., Wang, Y., Nishiyama, N., & Tomé, C. (2012). Texture and
632 elastic strains in hcp-iron plastically deformed up to 17.5 GPa and 600 K:
633 experiment and model. *Modelling and Simulation in Materials Science and*
634 *Engineering*, *20*(2), 024005. http://dx.doi.org/10.1088/0965-0393/20/2/024005
635 Miyagi, L., Kunz, M., Knight, J., Nasiatka, J., Voltolini, M., & Wenk, H.-R. (2008) *In*
636 *situ* phase transformation and deformation of iron at high pressure and temperature.
637 *Journal of Applied Physics*, *104*, 103510. https://doi.org/10.1063/1.3008035
638 Monnereau, M., Valvet, M., Margarin, L., & Souriau, A. (2010). Lopsided growth of
639 Earth's inner core. *Science*, *328*(5981), 1014-1017.
640 https://doi.org/10.1126/science.1186212
641 Morelli, A., Dziewonski, A.M., & Woodhouse, J.H. (1986). Anisotropy of the inner core
642 inferred from PKIKP travel times. *Geophysical Research Letters*, *13*(13), 1545-1548.
643 https://doi.org/10.1029/GL013i013p01545
644 Mukherjee, A.K. (2002). An examination of the constitutive equation for elevated
645 temperature plasticity. *Materials Science and Engineering: A*, *322*(1-2), 1-22.
646 https://doi.org/10.1016/S0921-5093(01)01115-7
647 Musienko, A., Tatschl, A., Schmidegg, K., Kolednik, O., Pippan, R., & Cailletaud, G.
648 (2007). Three-dimensional finite element simulation of a polycrystalline copper
649 specimen. *Acta Materialia*, *55*(12), 4121-4136.
650 https://doi.org/10.1016/j.actamat.2007.01.053

651 Nishihara, Y., Ohuchi, T., Kawazoe, T., Seto, Y., Maruyama, G., Higo, Y., Funakoshi, K.,
652 Tange, Y., & Irifune, T. (2018). Deformation-induced crystallographic-preferred
653 orientation of hcp-iron: An experimental study using a deformation-DIA apparatus.
654 *Earth and Planetary Science Letters*, *490*, 151-160.
655 https://doi.org/10.1016/j.epsl.2018.03.029
656 Nishihara, Y., Tsujino, N., Kubo, T., Yamazaki, D., Doi,S., Imamura, M., & Yoshino, T.
657 (2020a). Studies of deep Earth rheology based on high-Pressure deformation
658 experiments using D111-type apparatus. *The Review of High Pressure Science and*
659 *Technology*, *30*(2), 78-84 (in Japanese with English abstract).
660 https://doi.org/10.4131/jshpreview.30.78
661 Nishihara, Y., Doi, S., Kakizawa, S., Higo, Y., & Tange, Y. (2020b). Effect of pressure
662 on temperature measurements using WRe thermocouple and its geophysical impact.
663 *Physics of the Earth and Planetary Interiors*, 298, 106348.
664 https://doi.org/10.1016/j.pepi.2019.106348
665 Nishiyama, N., Wang, Y., Rivers, M.L., Sutton, S.R., & Cookson, D. (2007). Rheology
666 of ε-iron up to 19 GPa and 600 K in the D-DIA. *Geophysical Research Letters*,
667 *35*(23), L23304. https://doi.org/10.1029/2007GL031431
668 Nye, J.F., 1985. Physical Properties of Crystals, pp. 322, Oxford Univ. Press, New York.
669 Raterron, P., Merkel, S., & Holyoke, C.W. (2013). Axial temperature gradient and stress
670 measurements in the deformation-DIA cell using alumina pistons. *Review of*
671 *Scientific Instruments*, *84*(4), 043906. https://doi.org/10.1063/1.4801956
672 Reaman, D.M., Colijin, H.O., Yang, F., Hauser, A.J., & Panero, W.R. (2012).
673 Interdiffusion of Earth's core materials to 65 GPa and 2200 K. *Earth and Planetary*
674 *Science Letters*, *349-350*, 8-14. https://doi.org/10.1016/j.epsl.2012.06.053
675 Ritterbex, S., & Tsuchiya, T. (2020). Viscosity of hcp iron at Earth's inner core

676 conditions from density functional theory. *Scientific Reports*, *10*, 6311.
677 https://doi.org/10.1038/s41598-020-63166-6
678 Romanowicz, B., Cao, A., Godwal, B., Wenk, R., Ventosa, S., & Jeanloz, R. (2016).
679 Seismic anisotropy in the Earth's innermost inner core: testing structural models
680 against mineral physics predictions. *Geophysical Research Letters*, *43*(1), 93-100.
681 https://doi.org/10.1002/2015GL066734
682 Sakamaki, K., Takahashi, E., Nakajima, Y., Nishihara, Y., Funakoshi, K., Suzuki, T., &
683 Fukai, Y. (2009). Melting phase relation of FeH_x up to 20 GPa: Implication for the
684 temperature of the Earth's core. *Physics of the Earth and Planetary Interiors*,
685 *174*(1-4), 192-201. https://doi.org/10.1016/j.pepi.2008.05.017
686 Sata, N., Hirose, K., Shen, G., Nakajima, Y., Ohishi, Y., & Hirao, N. (2010).
687 Compression of FeSi, Fe_3C, $Fe_{0.95}O$, and FeS under the core pressures and
688 implication for light element in the Earth's core. *Journal of Geophysical Research:*
689 *Solid Earth*, *115*(B9), B09204. https://doi.org/10.1029/2009JB006975
690 Seto, Y., Nishio-Hamane, D., Nagai, T., & Sata, N. (2010). Development of a software
691 suite on X-ray diffraction experiments. *The Review of High Pressure Science and*
692 *Technology*, *20*(3), 269-276. https://doi.org/10.4131/jshpreview.20.269
693 Sha, X., & Cohen, R.E. (2010a). First-principles thermal equation of state and
694 thermoelasticity of hcp Fe at high pressures. *Physical Review B*, *81*, 094105.
695 https://doi.org/10.1103/PhysRevB.81.094105
696 Sha, X., & Cohen, R.E. (2010b). Elastic isotropy of ε-Fe under Earth's core conditions.
697 *Geophysical Research Letters*, *37*(10), L10302.
698 https://doi.org/10.1029/2009GL042224
699 Singh, A.K. (1993). The lattice strains in a specimen (cubic system) compressed
700 nonhydrostatically in an opposed anvil device. *Journal of Applied Physics*, *73*(9),

4278-4286. https://doi.org/10.1063/1.352809

Singh, A.K., Balasingh, C., Mao, H.-k., Hemley, R.J., & Shu, J. (1998). Analysis of lattice strains measured under nonhydrostatic pressure. *Journal of Applied Physics*, *83*(12), 7567-7575. https://doi.org/10.1063/1.367872

Souriau, A., & Calvet, M. (2015). Deep Earth structure: The Earth's cores, In B.A. Romanowicz (Ed.), *Treatise on Geophysics (Second Edition), Volume 1: Deep Earth Seismology*, (pp. 725-757) Amsterdam: Elsevier.

Sumita, I., & Bergman, M.I. (2009). Inner-core dynamics, In P. Olsen (Ed.), *Treatise on Geophysics, Volume 8: Core Dynamics*, (pp. 299-318) Amsterdam: Elsevier.

Tateno, S., Hirose, K., Ohishi, Y., & Tatsumi, Y. (2010). The structure of iron in Earth's inner core. *Science*, *330*(6002), 359-361. https://doi.org/10.1126/science.1194662

Thomson, A.R., Nishihara, Y., Yamazaki, D., Tsujino, N., Hunt, S.A., Tsubokawa, Y., Matsukage, K.N., Kubo, T., & Dobson, D. (2023). Preliminary results from the New Deformation multi-anvil press at the Photon Factory: insight into the creep strength of calcium silicate perovskite. In T. Nakagawa, M. Satish-Kumar, T. Tsuchiya (Eds.), *Core-Mantle Coevolution: A Multidisciplinary Approach*, Washington, DC: American Geophysical Union, in press.

Tsujino, N., Mârza, A., & Yamazaki, D. (2020). Pressure dependence of Si diffusion in γ-Fe. *American Mineralogist*, *105*(3), 319-324. https://doi.org/10.2138/am-2020-7197

Tsujino, N., Yamazaki, D., Nishihara, Y., Yoshino, T., Higo, Y., & Tange, Y. (2022). Viscosity of bridgmanite determined by in situ stress and strain measurements in uniaxial deformation experiments. *Science Advances*, *8*(13), eabm1821. https://doi.org/10.1126/sciadv.abm1821

Uchida, T., Funamori, N., & Yagi, T. (1996). Lattice strains in crystals under uniaxial

726 stress field. *Journal of Applied Physics*, *80*(2), 739-746.
727 https://doi.org/10.1063/1.362920
728 Uchida, T., Wang, Y., Rivers, M.L., & Sutton, S.R. (2001). Stability field and thermal
729 equation of state of ε-iron determined by synchrotron X-ray diffraction in a
730 multianvil apparatus. *Journal of Geophysical Research: Solid Earth*, *106*(B10),
731 21799-21810. https://doi.org/10.1029/2001JB000258
732 Van Orman, J.A. (2004). On the viscosity and creep mechanism of Earth's inner core.
733 *Geophysical Research Letters*, *31*(20), L20606.
734 https://doi.org/10.1029/2004GL021209
735 Wang, T., Song, X., & Xia, H.H. (2015). Equatorial anisotropy in the inner part of
736 Earth's inner core from autocorrelation of earthquake coda. *Nature Geoscience*, *8*,
737 224-227. https://doi.org/10.1038/ngeo2354
738 Wenk, H.-R., Matthies, S., Hemley, R.J., Mao, H.-k., & Shu, J. (2000) The plastic
739 deformation of iron at pressures of the Earth's inner core. *Nature*, *405*, 1044-1047.
740 https://doi.org/10.1038/35016558
741 Woodhouse, J.H., Giardini, D., & Li, X.-D. (1986). Evidence for inner core anisotropy
742 from free oscillations. *Geophysical Research Letters*, *13*(13), 1549-1552.
743 https://doi.org/10.1029/GL013i013p01549
744 Yamazaki, D., Ito, E., Yoshino, T., Yoneda, A., Guo, X., Zhang, B., Sun, W., Shimojuku,
745 A., Tsujino, N., Kunimoto, T., Higo, Y., & Funakoshi, K. (2012). P-V-T equation of
746 state for ε-iron up to 80 GPa and 1900 K using the Kawai-type high pressure
747 apparatus equipped with sintered. *Geophysical Research Letters*, *39*(20), L20308.
748 https://doi.org/10.1029/2012GL053540
749 Yamazaki, D., Tsujino, N., Yoneda, A., Ito, E., Yoshino, T., Tange, Y., & Higo, Y. (2017).
750 Grain growth of ε-iron: Implications to grain size and its evolution in the Earth's

751 inner core. *Earth and Planetary Science Letters*, *459*, 238-243.
752 https://doi.org/10.1016/j.epsl.2016.11.049
753 Yoshida, S., Sumita, I., & Kumazawa, M. (1996). Growth model of the inner core
754 coupled with outer core dynamics and the resulting elastic anisotropy. *Journal of*
755 *Geophysical Research: Solid Earth*, *101*(B12), 28085-28103.
756 https://doi.org/10.1029/96JB02700
757 Yunker, M.L., & Van Orman, J.A. (2007). Interdiffusion of solid iron and nickel at high
758 pressure. *Earth and Planetary Science Letters*, *254*(1-2), 203-213.
759 https://doi.org/10.1016/j.epsl.2006.11.036
760

761 **Figure captions**

762 Figure 1. Schematic illustrations of (a) 7M/2 assembly used in deformation experiments
763 with D111-type apparatus and (b) 4M/2.5 assembly used in deformation experiments
764 with D-DIA apparatus. The c- and d-Al_2O_3 are crushable- and dense-Al_2O_3, respectively.
765 The X-ray passed through perpendicular to page.

766

767 Figure 2. (a) X-ray radiograph at P = 16.3 GPa and T = 723 K with ε = 0.111 during
768 deformation in run Iron13 with D111-type apparatus. Sample and Al_2O_3 pistons were
769 visible through diagonal anvil gap (dashed lines indicate anvil surface). We determined
770 sample strain from distance of Au foil strain markers, which we placed at the top and
771 bottom ends of sample. (b) Plot of strain versus time for run Iron25. Run Iron25
772 included five tests at three different temperatures of 823 (step 1), 848 (step 2), and 873
773 (steps 3–5) K at nearly constant pressure (P = 16.5–17.5 GPa). In steps 3–5, strain rate
774 was changed stepwise.

775

776 Figure 3. Two-dimensional X-ray diffraction images of hcp-Fe (a) at P = 16.29 GPa and
777 T = 723 K with ε = 0.106 during deformation in run Iron13 using D111-type apparatus
778 and (b) at P = 17.52 GPa and T = 523 K with ε = 0.157 during deformation in run
779 M2609 using D-DIA apparatus. Compression direction is vertical. In (a), Diffraction
780 Debye rings were more intense at angles corresponding to anvil gap (from top right to
781 bottom left). In (b), the 0002 diffraction is more intense at top and bottom whereas the
782 $10\bar{1}0$ diffraction is at right and left which suggests basal plane normal is preferentially
783 oriented to compression axis. (c) Variation in d spacing of hcp-Fe $10\bar{1}0$ for run Iron13 at
784 P = 16.1–16.6 GPa. Open red circles, before deformation at T = 823 K; solid red circles,

785 green diamonds, and blue squares, during deformation at 823, 773, and 723 K,
786 respectively.
787
788 Figure 4. *P–T* conditions of deformation experiments. Open diamonds, inverse triangles,
789 and squares, conditions of stepped strain rate, stepped temperature, and stepped pressure
790 tests, respectively. Colored and black symbols, experiments using D111-type and
791 D-DIA apparatus, respectively. Attached numbers denote run numbers. Thick black
792 lines denote phase boundaries in Fe (Bundy, 1965; Uchida et al., 2001; Yamazaki et al.,
793 2012).
794
795 Figure 5. Plots of stress and pressure versus strain from deformation experiments (a)
796 Iron12 (stepped strain rate test), (b) Iron13 (stepped temperature test), (c) Iron14
797 (stepped pressure test), and (d) Iron25 (stepped temperature and strain rate test). Each
798 experiment included two or more deformation steps under different conditions. Error
799 bars for stress values represent errors in the fitting of Equation (1). Attached numbers
800 for each deformation step are strain rate in s^{-1}.
801
802 Figure 6. Plots of mechanical results. (a) Log-log plot of strain rate versus stress for
803 stepped strain rate tests. (b) Semilog plot of stress versus reciprocal temperature for
804 stepped temperature tests. (c) Semilog plot of stress versus pressure for stepped pressure
805 test. Symbols and error bars represent averages and ranges, respectively, of steady-state
806 stress determined from four diffraction peaks ($10\bar{1}0$, 0002, $10\bar{1}1$, and $10\bar{1}2$) except for
807 those in (c). Purple and black crosses in (a) are data at 600 and 400 K, respectively, at
808 15.9–17.5 GPa reported by Nishiyama et al. (2007) for which stress values are the
809 average of those of $10\bar{1}0$ and $10\bar{1}1$.

Figure 7. Results of (a, b) fit of flow-law equation for power-law creep (Equation (3)) to data at T = 823–873 K; (c, d) a simultaneous fit of flow-law equations for power-law creep and low-T creep (Equation (4)) to all data. All data were after stress correction for run-to-run variability, and were normalized to P = 17 GPa using parameters determined by fit of flow-law equations. Fit of flow-law equations is expressed by thick lines. Data of individual runs are connected by thin black dashed lines. (a, c) Log-log plots of strain rate versus stress including all data as symbols. Symbol and color indicate temperature. (b, d) Semi-log plots of stress versus reciprocal temperature including only data in stepped temperature tests as symbols for clarity. Experimental data were normalized to $\dot{\varepsilon} = 3 \times 10^{-6}$ (black) or 3×10^{-5} (red) s^{-1}. Attached small black numbers in (a, b) denote run numbers.

Figure 8. Extrapolation of flow-law of hcp-Fe for power-law creep to inner core conditions. Red lines are calculated stress–strain rate relationship for power-law creep at T_m/T = 2.28 and 1.1 based on our study (T_m/T = 2.28 corresponds to T = 873 K at 17 GPa). Dashed lines indicate range of 95% confidence level of extrapolation. Green lines are diffusion creep at T_m/T = 1.1 with grain size of d = 1 m, 10 m, 100 m, and 1 km calculated using Equation (6) and diffusion coefficient by Yunker and Van Orman (2007). Thin black lines are isopleths for viscosity (η) of 10^{12}, 10^{16}, 10^{20}, 10^{24}, and 10^{28} Pa s. Light blue area indicates range of stress in inner core, $<10^4$ Pa (Buffett, 1997, Karato, 1999, Yoshida et al., 1996). Thick blue line represents strain rate in inner core produced by equatorial inner core growth (Yoshida et al., 1996).

Figure.

Table 1
Experimental conditions and results

Run number		Pressure (GPa)	Temperature (K)	Strain	Strain rate (10^{-5} s^{-1})	Stress (GPa) $10\bar{1}0$	0002	$10\bar{1}1$	$10\bar{1}2$
Stepped strain rate tests									
Iron01	-1	17.36	823	0.011	0.15	0.49 ± 0.03	0.36 ± 0.02	0.37 ± 0.02	0.32 ± 0.04
	-2	17.26	823	0.017	0.55	0.67 ± 0.03	0.55 ± 0.03	0.46 ± 0.02	0.37 ± 0.03
Iron11	-1	22.57	823	0.017	0.37	0.58 ± 0.05	0.58 ± 0.05	0.52 ± 0.03	0.47 ± 0.06
	-2	22.18	823	0.013	0.75	0.80 ± 0.05	0.79 ± 0.06	0.62 ± 0.03	0.55 ± 0.04
Iron12	-1	17.29	823	0.024	0.41	1.09 ± 0.08	0.90 ± 0.07	0.72 ± 0.04	0.67 ± 0.05
	-2	16.84	823	0.020	1.36	1.43 ± 0.08	1.14 ± 0.07	0.82 ± 0.04	0.71 ± 0.05
	-3	16.49	823	0.031	5.09	1.51 ± 0.07	1.18 ± 0.06	0.86 ± 0.03	0.64 ± 0.07
Iron26	-1	16.99	873	0.025	0.98	0.34 ± 0.03	0.28 ± 0.03	0.29 ± 0.02	0.29 ± 0.02
	-2	17.05	873	0.016	0.57	0.32 ± 0.03	0.26 ± 0.03	0.27 ± 0.02	0.26 ± 0.02
	-3	16.94	873	0.018	0.35	0.29 ± 0.03	0.24 ± 0.03	0.24 ± 0.03	0.24 ± 0.02
	-4	16.83	873	0.040	1.82	0.49 ± 0.04	0.40 ± 0.04	0.38 ± 0.03	0.34 ± 0.02
	-5	16.65	873	0.059	4.16	0.58 ± 0.05	0.47 ± 0.04	0.44 ± 0.04	0.37 ± 0.03
M2190	-1	17.19	723	0.062	0.79	1.95 ± 0.03	1.42 ± 0.04	1.25 ± 0.03	0.92 ± 0.02
	-2*	16.96	723	0.093	4.14	2.05 ± 0.03	1.49 ± 0.04	1.33 ± 0.03	0.91 ± 0.02
Stepped temperature tests									
Iron06	-1	17.21	823	0.032	0.57	0.68 ± 0.04	0.54 ± 0.04	0.50 ± 0.02	0.46 ± 0.04
	-2	17.07	773	0.020	0.76	1.08 ± 0.04	0.93 ± 0.04	0.71 ± 0.02	0.60 ± 0.04
	-3	16.87	723	0.023	0.90	1.38 ± 0.04	1.24 ± 0.05	0.87 ± 0.02	0.71 ± 0.04
Iron13	-1	16.48	823	0.032	1.69	0.75 ± 0.03	0.61 ± 0.03	0.60 ± 0.04	0.56 ± 0.09
	-2	16.50	773	0.034	2.26	1.19 ± 0.06	1.02 ± 0.05	0.79 ± 0.03	0.69 ± 0.08
	-3	16.25	723	0.045	2.91	1.62 ± 0.07	1.36 ± 0.06	0.96 ± 0.03	0.81 ± 0.12
Iron17	-1	20.62	923	0.014	0.89	-	-	-	-
	-2	20.26	873	0.029	1.42	0.47 ± 0.08	0.31 ± 0.07	0.33 ± 0.03	0.19 ± 0.07
	-3	19.90	823	0.047	2.08	0.91 ± 0.09	0.72 ± 0.08	0.56 ± 0.03	0.37 ± 0.07
M2606	-1	17.18	723	0.030	0.79	1.95 ± 0.02	1.59 ± 0.04	1.25 ± 0.03	0.97 ± 0.01
	-2	17.44	623	0.018	0.75	2.69 ± 0.02	2.03 ± 0.09	1.70 ± 0.04	1.25 ± 0.02
	-3	17.58	523	0.021	0.87	2.96 ± 0.03	2.34 ± 0.11	1.86 ± 0.05	1.36 ± 0.02
	-4	17.74	423	0.027	1.09	2.96 ± 0.04	2.62 ± 0.12	1.87 ± 0.05	1.36 ± 0.02
Stepped pressure tests									
Iron14	-1	16.56	823	0.039	1.31	0.99 ± 0.04	0.81 ± 0.04	0.65 ± 0.02	0.60 ± 0.03
	-2	21.35	823	0.031	1.12	1.16 ± 0.04	1.09 ± 0.04	0.77 ± 0.02	0.68 ± 0.04
Others									
Iron25	-1	17.50	823	0.031	0.92	0.66 ± 0.05	0.53 ± 0.03	0.50 ± 0.02	0.45 ± 0.04
	-2	17.41	848	0.027	1.26	0.56 ± 0.05	0.44 ± 0.03	0.43 ± 0.02	0.39 ± 0.04
	-3	17.13	873	0.028	1.52	0.46 ± 0.04	0.35 ± 0.03	0.35 ± 0.02	0.34 ± 0.04
	-4	16.80	873	0.040	3.87	0.57 ± 0.05	0.43 ± 0.03	0.42 ± 0.02	0.38 ± 0.04
	-5	16.50	873	0.056	8.81	0.69 ± 0.05	0.51 ± 0.04	0.48 ± 0.02	0.41 ± 0.04
M2609	-1	16.92	623	0.023	0.51	2.70 ± 0.03	2.22 ± 0.07	1.68 ± 0.04	1.32 ± 0.02
	-2	17.53	623	0.042	2.58	2.86 ± 0.03	1.98 ± 0.10	1.80 ± 0.05	1.32 ± 0.02
	-3	17.62	523	0.035	0.69	3.07 ± 0.03	2.58 ± 0.09	1.95 ± 0.05	1.43 ± 0.02
	-4	17.56	523	0.054	3.04	2.87 ± 0.06	2.65 ± 0.08	1.81 ± 0.05	1.23 ± 0.03

Runs with series of run number "Iron" are conducted using D111-type apparatus, and those with series of run number "M" are using D-DIA.

* Temperature was dropped to ~400 K instantaneously and recovered to 723 K within a few seconds.

Table 2
Flow law parameters

Parameters		Power-law creep (PL)			Low-T creep (LT)
$\log_{10}A$	(s^{-1} GPa^{-n})	12.5	±	1.6	5.4
n		4.0	±	0.3	5
E^*	(kJ/mol)	240	±	20	148[a]
V^*	(cm^3/mol)	1.4	±	0.2	0.90[a]
σ_P	(GPa)		-		2.3
p			-		1
q			-		0.1

a: Parameters for boundary diffusion coefficient after Brown and Ashby (1980). Parameters for power-law and low-T creeps are for Equations (2) and (4), respectively. See text for details.

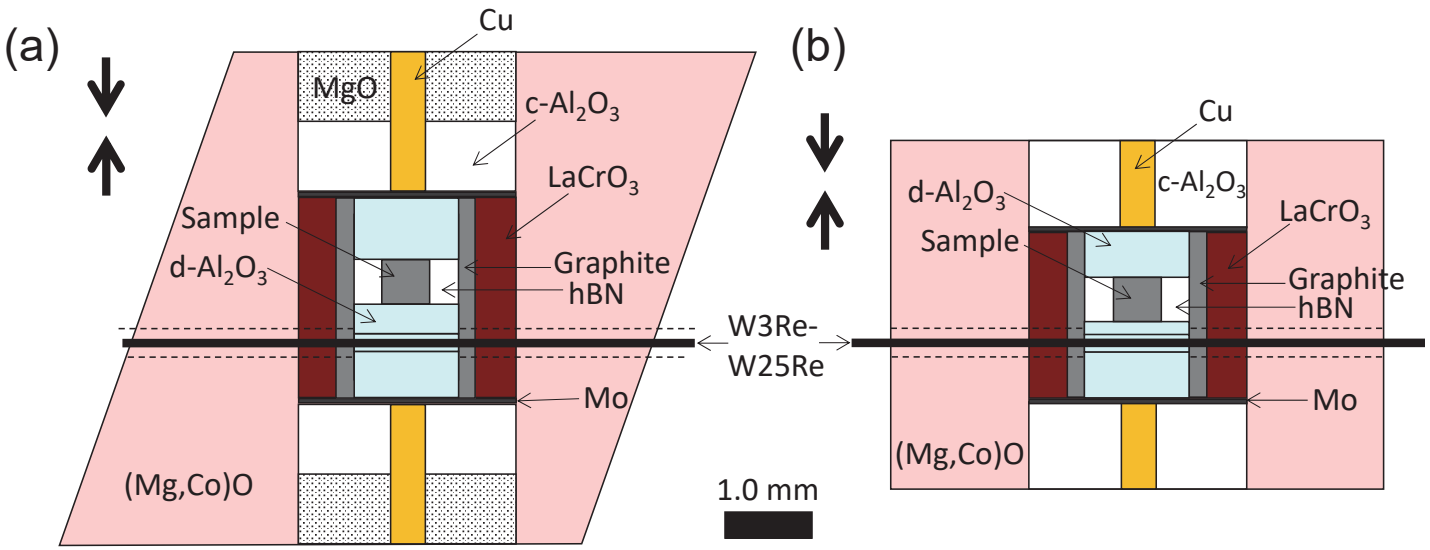

Figure 1. Schematic illustrations of (a) 7M/2 assembly used in deformation experiments with D111-type apparatus and (b) 4M/2.5 assembly used in deformation experiments with D-DIA apparatus. The c- and d-Al_2O_3 are crushable- and dense-Al_2O_3, respectively. The X-ray passed through perpendicular to page.

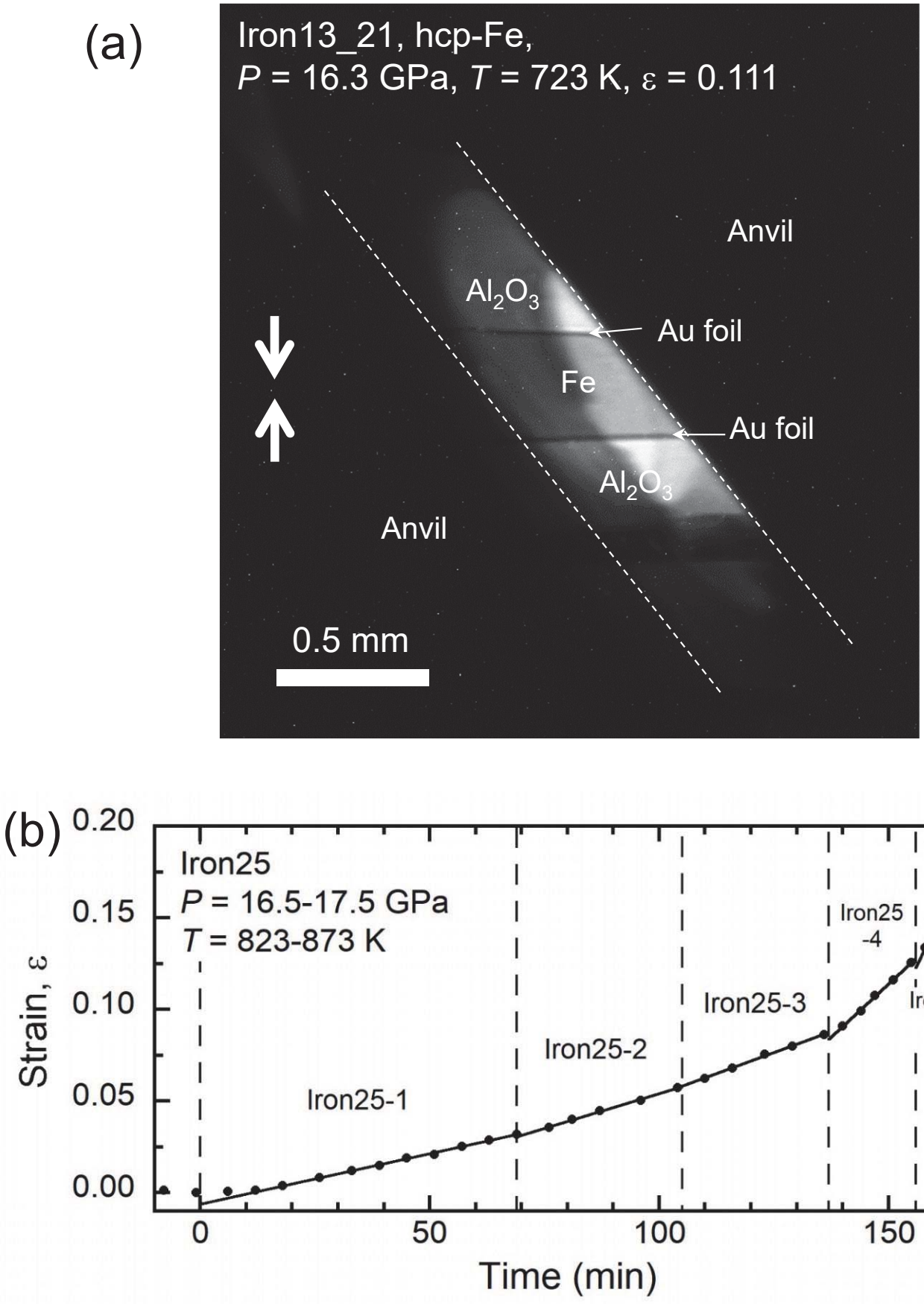

Figure 2. (a) X-ray radiograph at P = 16.3 GPa and T = 723 K with ε = 0.111 during deformation in run Iron13 with D111-type apparatus. Sample and Al_2O_3 pistons were visible through diagonal anvil gap (dashed lines indicate anvil surface). We determined sample strain from distance of Au foil strain markers, which we placed at the top and bottom ends of sample. (b) Plot of strain versus time for run Iron25. Run Iron25 included five tests at three different temperatures of 823 (step 1), 848 (step 2), and 873 (steps 3–5) K at nearly constant pressure (P = 16.5–17.5 GPa). In steps 3–5, strain rate was changed stepwise.

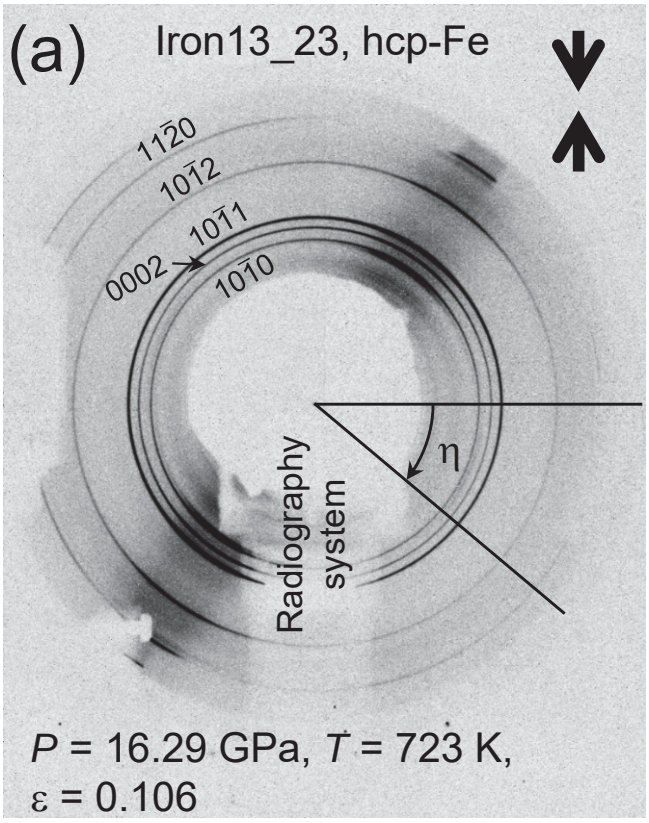

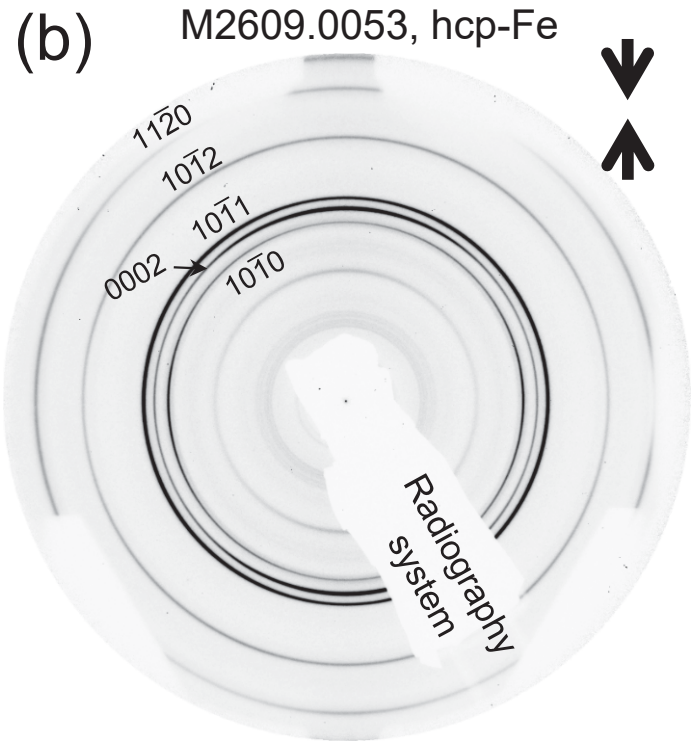

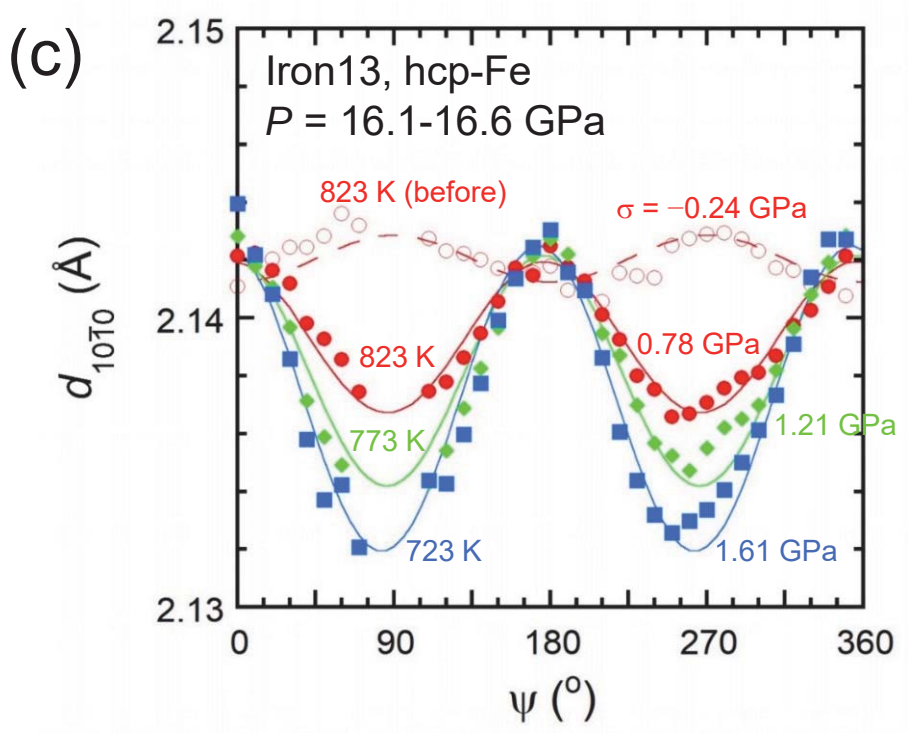

Figure 3. Two-dimensional X-ray diffraction images of hcp-Fe (a) at P = 16.29 GPa and T = 723 K with ε = 0.106 during deformation in run Iron13 using D111-type apparatus and (b) at P = 17.52 GPa and T = 523 K with ε = 0.157 during deformation in run M2609 using D-DIA apparatus. Compression direction is vertical. In (a), diffraction Debye rings were more intense at angles corresponding to anvil gap (from top right to bottom left). In (b), the 0002 diffraction is more intense at top and bottom whereas the 10$\bar{1}$0 diffraction is at right and left which suggests basal plane normal is preferentially oriented to compression axis. (c) Variation in d spacing of hcp-Fe 10$\bar{1}$0 for run Iron13 at P = 16.1–16.6 GPa. Open red circles, before deformation at T = 823 K; solid red circles, green diamonds, and blue squares, during deformation at 823, 773, and 723 K, respectively.

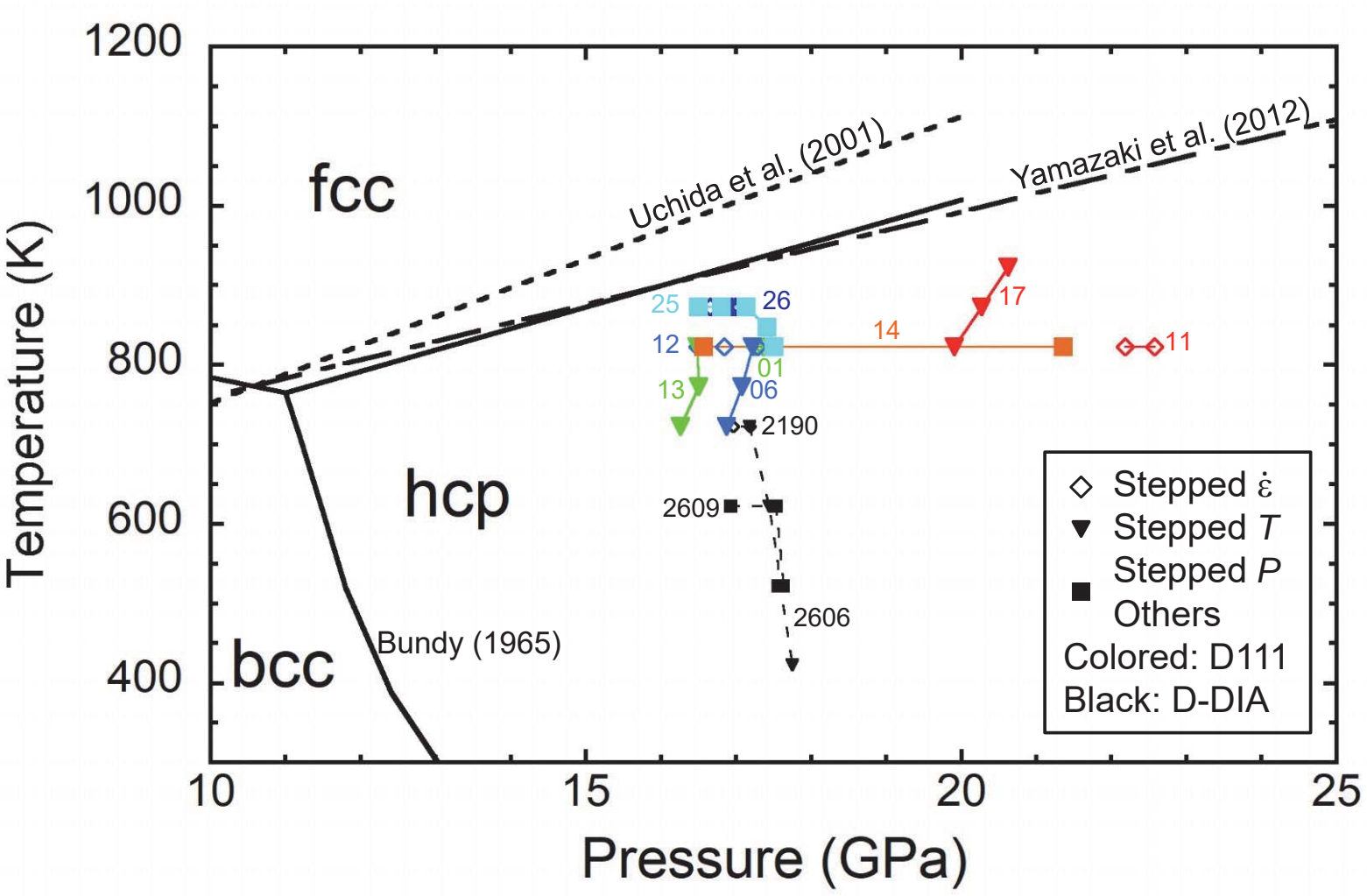

Figure 4. *P–T* conditions of deformation experiments. Open diamonds, inverse triangles, and squares, conditions of stepped strain rate, stepped temperature, and stepped pressure tests, respectively. Colored and black symbols, experiments using D111-type and D-DIA apparatus, respectively. Attached numbers denote run numbers. Thick black lines denote phase boundaries in Fe (Bundy, 1965; Uchida et al., 2001; Yamazaki et al., 2012).

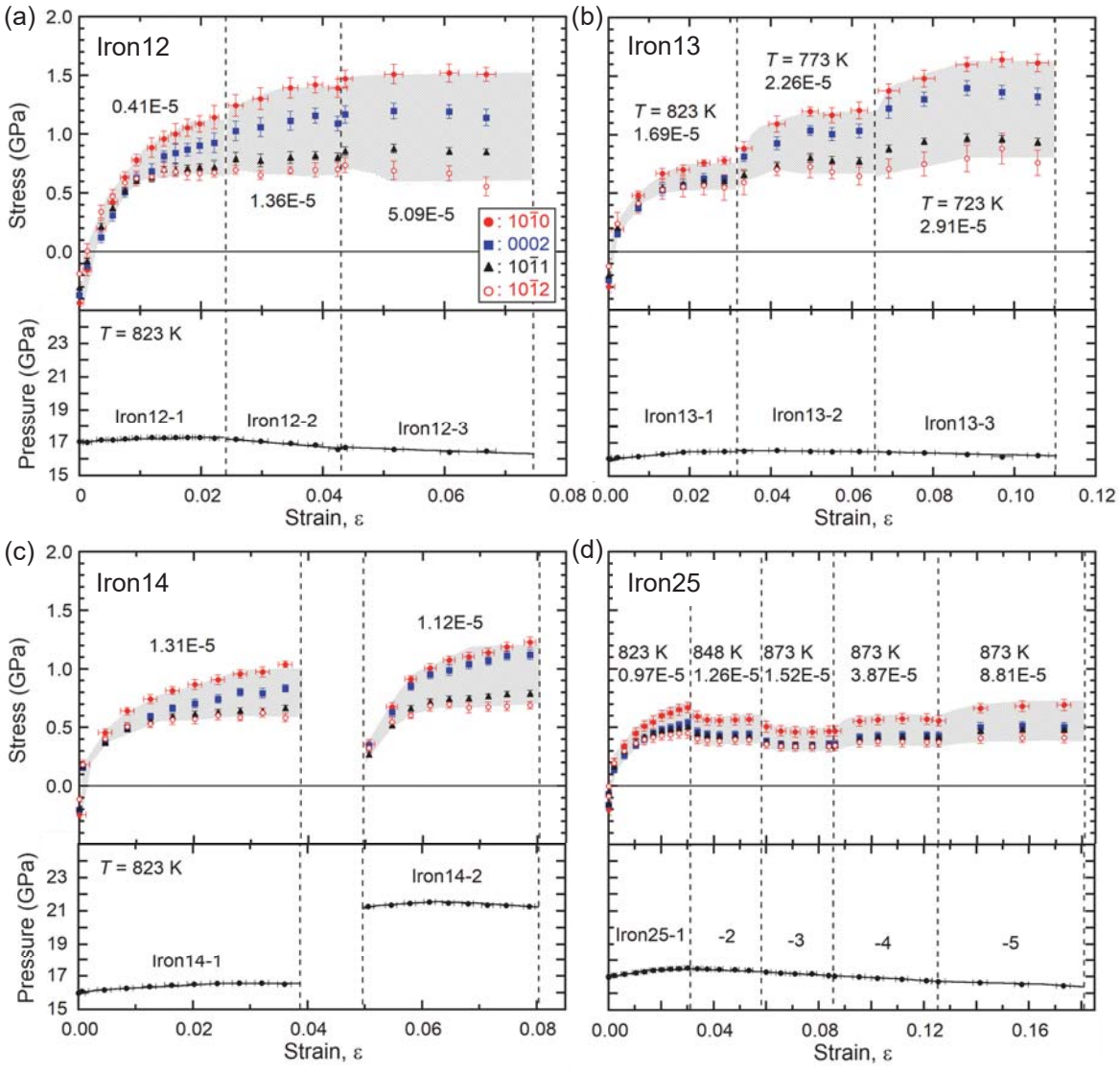
(a)
Iron12
0.41E-5
1.36E-5
5.09E-5
●: 10$\bar{1}$0
■: 0002
▲: 10$\bar{1}$1
○: 10$\bar{1}$2
Stress (GPa)
T = 823 K
Iron12-1
Iron12-2
Iron12-3
Pressure (GPa)
Strain, ε
(b)
Iron13
T = 773 K
2.26E-5
T = 823 K
1.69E-5
T = 723 K
2.91E-5
Iron13-1
Iron13-2
Iron13-3
Strain, ε
(c)
Iron14
1.31E-5
1.12E-5
T = 823 K
Iron14-1
Iron14-2
Strain, ε
(d)
Iron25
823 K
0.97E-5
848 K
1.26E-5
873 K
1.52E-5
873 K
3.87E-5
873 K
8.81E-5
Iron25-1
-2
-3
-4
-5
Strain, ε

Figure 5

Figure 5. Plots of stress and pressure versus strain from deformation experiments (a) Iron12 (stepped strain rate test), (b) Iron13 (stepped temperature test), (c) Iron14 (stepped pressure test), and (d) Iron25 (stepped temperature and strain rate test). Each experiment included two or more deformation steps under different conditions. Error bars for stress values represent errors in the fitting of Equation (1). Attached numbers for each deformation step are strain rate in s^{-1}.

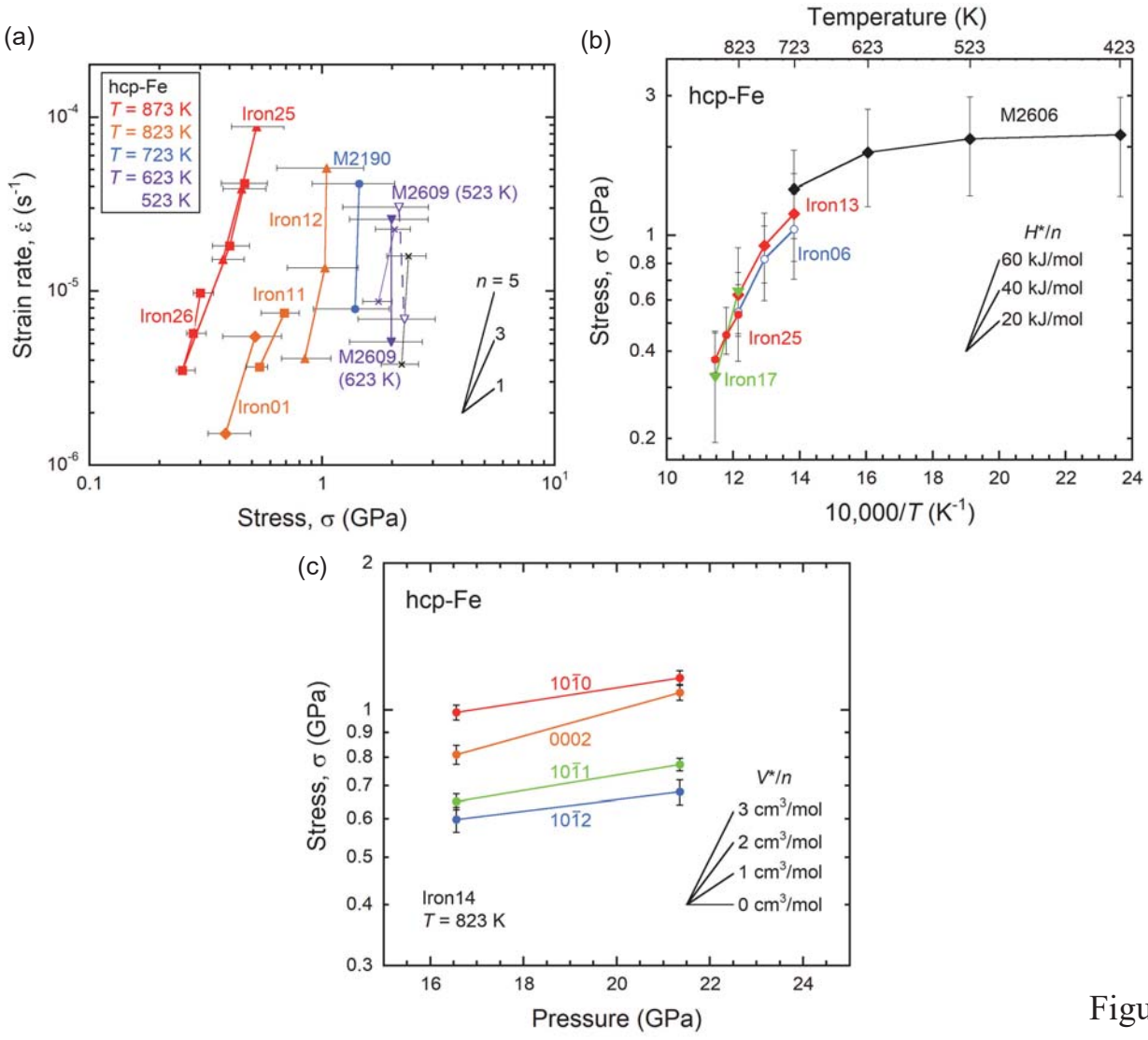
(a)
hcp-Fe
T = 873 K
T = 823 K
T = 723 K
T = 623 K
523 K
Iron25
M2190
M2609 (523 K)
Iron12
Iron11
Iron26
M2609 (623 K)
Iron01
n = 5
3
1
Strain rate, ε̇ (s⁻¹)
Stress, σ (GPa)
(b)
Temperature (K)
hcp-Fe
M2606
Iron13
Iron06
Iron25
Iron17
H*/n
60 kJ/mol
40 kJ/mol
20 kJ/mol
Stress, σ (GPa)
10,000/T (K⁻¹)
(c)
hcp-Fe
10$\bar{1}$0
0002
10$\bar{1}$1
10$\bar{1}$2
V*/n
3 cm³/mol
2 cm³/mol
1 cm³/mol
0 cm³/mol
Iron14
T = 823 K
Stress, σ (GPa)
Pressure (GPa)

Figure 6

Figure 6. Plots of mechanical results. (a) Log-log plot of strain rate versus stress for stepped strain rate tests. (b) Semilog plot of stress versus reciprocal temperature for stepped temperature tests. (c) Semilog plot of stress versus pressure for stepped pressure test. Symbols and error bars represent averages and ranges, respectively, of steady-state stress determined from four diffraction peaks ($10\bar{1}0$, 0002, $10\bar{1}1$, and $10\bar{1}2$) except for those in (c). Purple and black crosses in (a) are data at 600 and 400 K, respectively, at 15.9–17.5 GPa reported by Nishiyama et al. (2007) for which stress values are the average of those of $10\bar{1}0$ and $10\bar{1}1$.

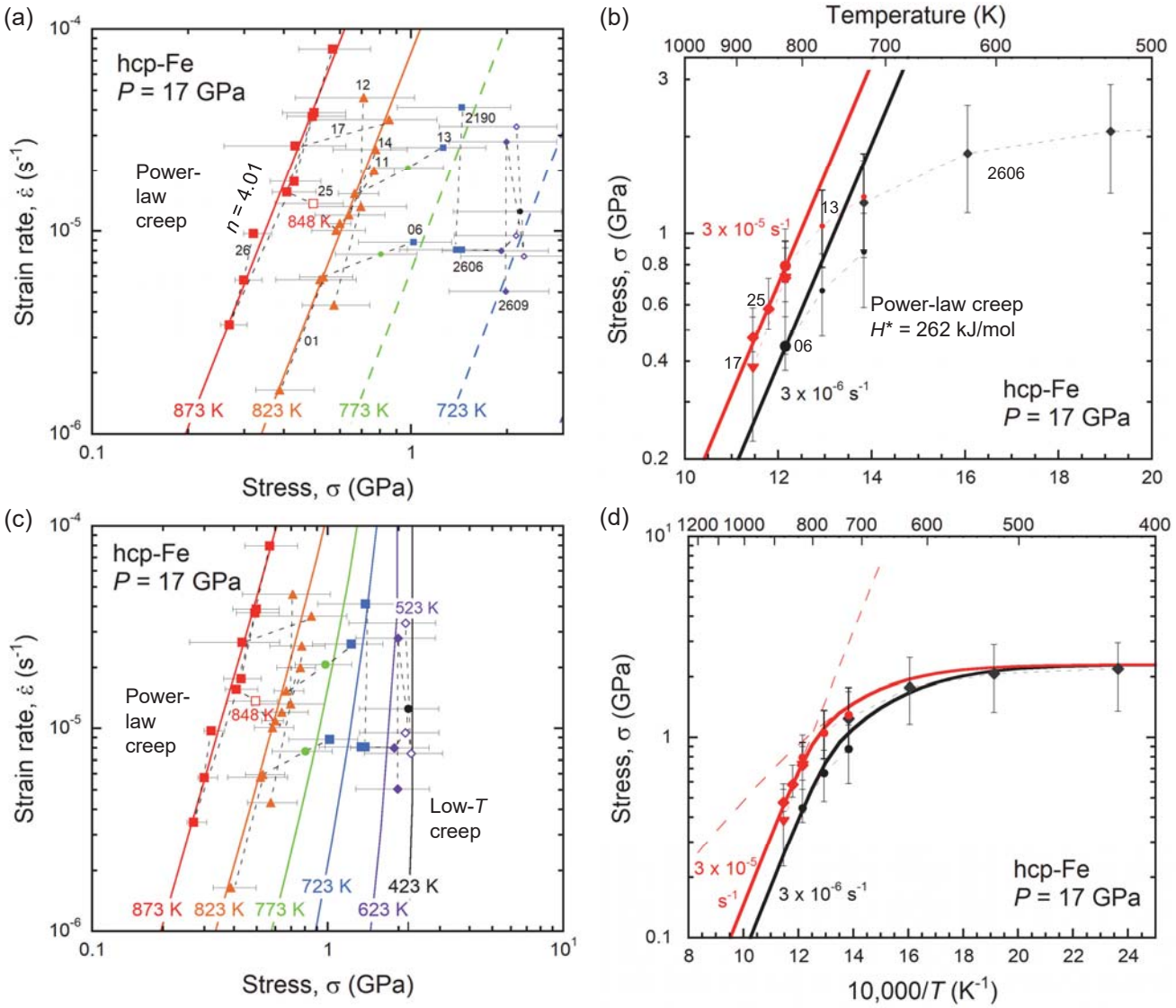
(a)
hcp-Fe
P = 17 GPa
Power-law creep
n = 4.01
848 K
873 K
823 K
773 K
723 K
Strain rate, ε̇ (s⁻¹)
Stress, σ (GPa)
(b)
Temperature (K)
Stress, σ (GPa)
3 x 10⁻⁵ s⁻¹
3 x 10⁻⁶ s⁻¹
Power-law creep
H* = 262 kJ/mol
hcp-Fe
P = 17 GPa
(c)
hcp-Fe
P = 17 GPa
Power-law creep
Low-T creep
873 K
823 K
773 K
723 K
623 K
523 K
423 K
Strain rate, ε̇ (s⁻¹)
Stress, σ (GPa)
(d)
Stress, σ (GPa)
3 x 10⁻⁵ s⁻¹
3 x 10⁻⁶ s⁻¹
hcp-Fe
P = 17 GPa
10,000/T (K⁻¹)

Figure 7

Figure 7. Results of (a, b) fit of flow-law equation for power-law creep (Equation (3)) to data at T = 823–873 K; (c, d) a simultaneous fit of flow-law equations for power-law creep and low-T creep (Equation (4)) to all data. All data were after stress correction for run-to-run variability, and were normalized to P = 17 GPa using parameters determined by fit of flow-law equations. Fit of flow-law equations is expressed by thick lines. Data of individual runs are connected by thin black dashed lines. (a, c) Log-log plots of strain rate versus stress including all data as symbols. Symbol and color indicate temperature. (b, d) Semi-log plots of stress versus reciprocal temperature including only data in stepped temperature tests as symbols for clarity. Experimental data were normalized to $\dot{\varepsilon} = 3 \times 10^{-6}$ (black) or 3×10^{-5} (red) s^{-1}. Attached small black numbers in (a, b) denote run numbers.

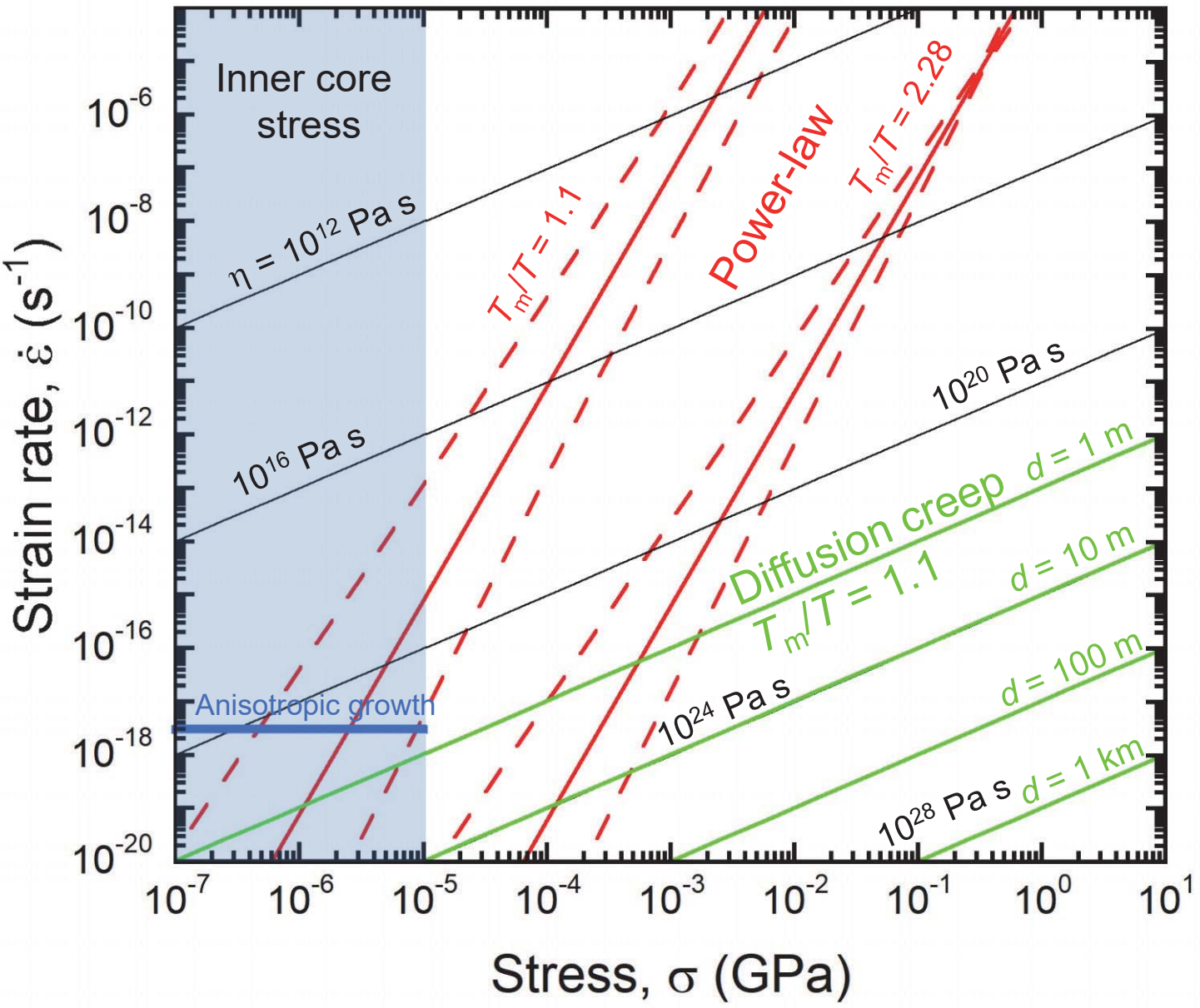

Figure 8. Extrapolation of flow-law of hcp-Fe for power-law creep to inner core conditions. Red lines are calculated stress–strain rate relationship for power-law creep at T_m/T = 2.28 and 1.1 based on our study (T_m/T = 2.28 corresponds to T = 873 K at 17 GPa). Dashed lines indicate range of 95% confidence level of extrapolation. Green lines are diffusion creep at T_m/T = 1.1 with grain size of d = 1 m, 10 m, 100 m, and 1 km calculated using Equation (5) and diffusion coefficient by Yunker and Van Orman (2007). Thin black lines are isopleths for viscosity (η) of 10^{12}, 10^{16}, 10^{20}, 10^{24}, and 10^{28} Pa s. Light blue area indicates range of stress in inner core, $<10^4$ Pa (Buffett, 1997, Karato, 1999, Yoshida et al., 1996). Thick blue line represents strain rate in inner core produced by anisotropic inner core growth (Yoshida et al., 1996).